OXFORD

Journal of Petrology, 2023, **64**, 1–20
https://doi.org/10.1093/petroj/egad011
Advance access publication date 17 February 2023
Original Manuscript

Multiple Episodes of Rock-Melt Reaction at the Slab-Mantle Interface: Formation of High Silica Primary Magmas in Intermediate to Hot Subduction Zones

Anna M. Rebaza[1,*] and Ananya Mallik[1] and Susanne M. Straub[2]

[1]Department of Geosciences,University of Arizona, 1040 E 4th St, Tucson, AZ 85721, USA
[2]Lamont-Doherty Earth Observatory, Columbia University, 61 Rte 9W, Palisades, NY 10964, USA

*Corresponding author: E-mail: arebaza@arizona.edu

Abstract

Siliceous slab-derived partial melts infiltrate the sub-arc mantle and cause rock-melt reactions, which govern the formation of diverse primary arc magmas and lithological heterogeneities. The effect of bulk water content, composition of reactants, and nature of melt infiltration (porous versus channelized) on the rock-melt reactions at sub-arc conditions have been investigated by previous studies. However, the effect of multiple episodes of rock-melt reactions in such scenarios has not been investigated before. Here, we explore mantle wedge modifications through serial additions of hydrous-silicic slab partial melts and whether such a process may ultimately explain the origin of high-Mg# andesites found in arcs worldwide. A series of piston-cylinder experiments simulate a serial addition of silicic slab melts in up to three stages (I through III) at 3 GPa and 800–1050°C, using rock-melt proportions of 75–25 and 50–50. A synthetic KLB-1 and a natural rhyolite (JR-1) represented the mantle and the slab components, respectively. Right from the first rock-melt interaction, the peridotite mantle transforms into olivine-free mica-rich pyroxenites ± amphibole ± quartz/coesite in equilibrium with rhyolitic-hydrous melts (72–80 wt% SiO_2 and 40–90 Mg#). The formation of olivine-free pyroxenite seems to be controlled by complex functions of T, P, rock-melt ratio, wedge composition, and silica activity of the slab-melt. Remarkably, the pyroxenites approach a melt-buffered state with progressive stages of rock-melt reactions, where those rhyolitic melts inherit and preserve the major (alkalis, Fe, Mg, Ca) and trace element slab-signature. Our results demonstrate that lithological heterogeneities such as pyroxenites formed as products of rock-melt reactions in the sub-arc mantle may function as melt 'enablers,' implying that they may act as pathways that enable the infiltrating melt to retain their slab signature without undergoing modification. Moreover, the density contrast between the products of rock-melt reaction (melts and residues) and the average mantle wedge (~150 to 400 kg/m^3) may help forming instabilities and diapiric rise of the slab components into the mantle wedge. However, the fate of the primitive slab-melts seems to be associated with the length of the pathway of mantle interaction which explains the evident wide magma spectrum as well as their degree of slab garnet-signature dilution. This work and the existence of high-Mg# Mexican-trondhjemites indicates that almost pristine slab-melts can make their way up to crustal levels and contribute to the arc magma diversity.

Keywords: pyroxenites, subduction zones, slab-mantle interface, high-silica primary magmas, multiple rock-melt reactions, high-Mg# andesites

INTRODUCTION

Subduction zones produce unique 'arc magmas', which stand out by their high SiO_2 contents (>60 wt%) relative to mid-ocean ridge basalts (MORBs) along with enriched H_2O (up to >10 wt% H_2O, (Anderson, 1974; Carmichael, 2002; Grove *et al.*, 2002; Ruscitto *et al.*, 2012; Plank *et al.*, 2013; Goltz *et al.*, 2020) and LILE contents (e.g. Hawkesworth *et al.*, 1993; Plank & Langmuir, 1993; Miller & Goldstein, 1994; Elliott *et al.*, 1997). A larger subgroup of the arc magmas have high-Mg# values of >60 [Mg# - molar ratio of Mg/(Mg + Fe2+)] (Fig. 1), and are referred to as high-Mg# andesites (Kelemen *et al.*, 2014). They are present in non-negligible amounts in many arcs, such as the Trans-Mexican Volcanic Belt (Gómez-Tuena *et al.*, 2018a), Kamchatka (Bindeman *et al.*, 2004; Portnyagin *et al.*, 2007; Bryant *et al.*, 2011), New Zealand (Cameron *et al.*, 2010; Price *et al.*, 2012; Beier *et al.*, 2017), the Western Aleutians (Kelemen *et al.*, 2014; Yogodzinski *et al.*, 2015) and the Cascades (Bullen & Clynne, 1990; Borg *et al.*, 1997; Grove *et al.*, 2002; Sisson *et al.*, 2014). Because high-Mg# andesites are often relatively rich in Ni (>100 ppm) and Cr (>300 ppm) and crystallize forsteritic Cr-spinel-bearing olivines (e.g. Kelemen *et al.*, 2014; Tatsumi & Ishizaka, 1982; Yogodzinski *et al.*, 1994; Martin *et al.*, 2005), an origin as primary mantle melts has been proposed (Tatsumi, 1982; Yogodzinski *et al.*, 1994; Kelemen, 1995). Low degree partial melting experiments on hydrous peridotites (≤10% melt) produced melts with as much as 60 wt% SiO_2 (e.g. Kushiro, 1972; Baker & Stolper, 1994; Hirose & Kawamoto, 1995; Hirose, 1997; Wood & Turner, 2009; Grove *et al.*, 2012) and high-Mg# (>70) (Grove & Till, 2019). Gómez-Tuena *et al.* (2014) pointed out that the last high-SiO_2 melt equilibration can only form at a low temperature ($T < 1000$°C) and pressures ($P = 1$ GPa), high melt water (> 7w% H_2O) and by reacting with harzburgitic mantle residues. However, these conditions rarely converge in nature, and are inconsistent

Received: April 8, 2022. **Revised:** February 2, 2023. **Accepted:** February 9, 2023
Published by Oxford University Press 2023.

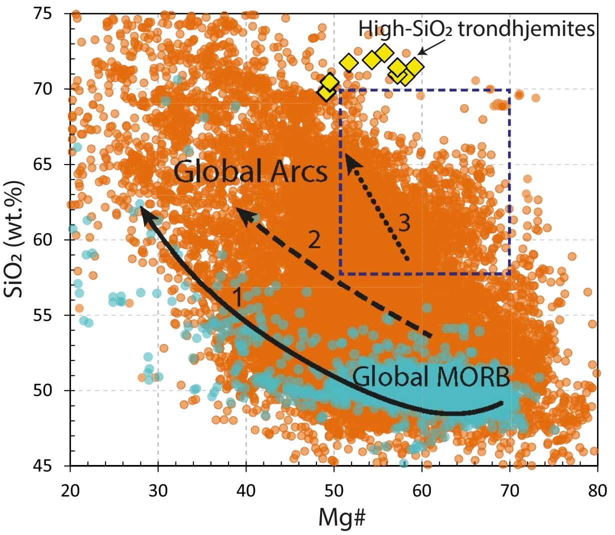

Fig. 1. SiO_2 wt% vs. Mg# of 12 656 global arc magmas relative to 2382 global MORBs, which represent partial melts from upper mantle unaffected by subduction. The global MORBs are from Gale *et al.* (2013) and the global arc magma compilations are from Straub (2017 and 2019) and re-compiled from GeoROC Database (https://georoc.eu/). High-silica intrusive trondhjemites (yellow diamonds) are from Gómez-Tuena *et al.*, (2008). The dashed square defines the arc lavas of interest that display high-SiO_2 and high-Mg#. The solid and dashed lines (1 and 2) represent the two liquid lines of descent at 1 GPa for a natural hydrous high-Mg basalt (Ulmer *et al.*, 2018) and for a high-alumina quartz tholeiite (Green & Ringwood, 1967), respectively. The dotted line (3) represents the experimental liquid trend of reaction between hydrous silicic melts (5 wt% H_2O) and peridotite at 1.5 GPa (Carroll & Wyllie, 1989) that would occur near the crust–mantle boundary (950–1100°C). The arrows indicate the direction toward lower *T* (from 1230 to 750°C in path 1 and 1040 to 920°C in path 2).

with geological observations [e.g. high-Mg# andesites erupts through ~40 km thick crust (Gómez-Tuena *et al.*, 2018a)], and such low degree partial melts are likely volumetrically too small to form the non-negligible amounts of high-SiO_2 and high-Mg# arc lavas mentioned above. Crustal processing of basaltic mantle melts mostly also cannot produce typical high-Mg# andesites (Kelemen, 1995; Kelemen *et al.*, 2014). Fractional crystallization of hydrous basaltic (e.g. Ulmer *et al.*, 2018; Fig. 1, path 1) or high-alumina quartz tholeiite melts (e.g. Green & Ringwood, 1967; Fig. 1, path 2) at shallower depths (<1 GPa) produces liquid lines of descent that show a consistent inverse relationship between Mg# and SiO_2. Only the reaction between hydrous silicic melts and peridotite (Carroll & Wyllie, 1989; Fig. 1, path 3) show an increase in SiO_2 with relatively less variations in Mg#. Thus, high-Mg# andesites produced by hydrous peridotite melting or via crustal processing alone should be very rare.

An alternative group of models has long proposed that infiltration of silicic slab components into the peridotitic mantle wedge leads to primary high-Mg# andesite formation (e.g. Ringwood, 1974; Straub *et al.*, 2011; Kelemen *et al.*, 2014; Parolari *et al.*, 2018). Because silicic slab materials and peridotite are out of equilibrium, the infiltration must be highly reactive and may result in a network of secondary pyroxenite veins or other segregations along the infiltrations paths in the peridotite (Hauri, 1996; Yaxley & Green, 1998; Rapp *et al.*, 1999; Straub *et al.*, 2011; Mallik & Dasgupta, 2012). Secondary pyroxenites are not only more fusible than the peridotite, they can, if oversaturated in SiO_2, generate primary high-Mg# dacitic melts (Hauri, 1996; Kogiso *et al.*, 2004). Such dacitic melts may then mix en-route to surface with basaltic components from surrounding lithologies (peridotite or silica-deficient pyroxenite) to form intermediate high-Mg# andesites (Straub *et al.*, 2011). In fact, the concept of olivine-free pyroxenitic lithologies in the sub-arc mantle (Straub *et al.*, 2008; Bryant *et al.*, 2011; Díaz-Bravo *et al.*, 2014; Søager *et al.*, 2015; Zamboni *et al.*, 2017) seems to be supported by the discovery of 'high-Ni olivines' in arc magmas which are olivine with Ni content higher than plausible for partial melts of peridotite (Sobolev *et al.*, 2005). Moreover, silicic slab melts, and more recently diapirs composed by recycled crustal materials have been suggested to be responsible for trace element recycling (H_2O and LILE) in global arcs (Li *et al.*, 2022), implying that slab signature flux is causally related to those high-SiO_2 arc magmas (Kelemen *et al.*, 2014; Straub *et al.*, 2014a; Parolari *et al.*, 2021).

Several experimental studies explored the reactive slab-mantle hybridization which typically involves two end member components (representing mantle and slab) at variable H_2O contents, and *P* and *T* relevant for the conditions of the mantle wedge. The slab end member is generally approximated by sediments or partial melts of continental or marine sediments (Sekine & Wyllie, 1983; Mallik *et al.*, 2015, 2016; Pirard & Hermann, 2015; Förster *et al.*, 2017, 2019; Wang & Foley, 2018; Zhang *et al.*, 2020b), subducted oceanic crustal metabasalts (Rapp & Watson, 1995; Rapp *et al.*, 1999; Lara & Dasgupta, 2020), and K-rich hydrous melts (Grove & Till, 2019). The mantle wedge end member is normally approximated by lherzolite, harzburgite or dunite. Two experimental setups of one single-step rock-melt reaction have been used for decades: (a) 'porous flow' which means reaction on the microscale induced by thorough physical mixing of the endmembers and simulated by using mixed powders; and (b) 'focused flow' which refers to reaction between melt and wall-rock in veins and fractures and is simulated by placing a felsic slab-derived melt and a peridotite in contact (layered geometry). Both setups show an effective hybridization reaction of the two components, but such mechanisms have limitations as to how, and how extensively, the slab melts can infiltrate the mantle and transfer the slab-signature to the arc lavas. The 'Porous flow' mechanism leads to extensive reaction with the mantle that modifies not only the major element composition but also the slab trace pattern (e.g. Pirard & Hermann, 2015). 'Focused flow' seems to be a viable mechanism for slab-melts to infiltrate farther into the mantle wedge, but its reaction forms ortho-pyroxenite 'barriers' that prevents further slab-melt infiltration (e.g. Lambart *et al.*, 2012, 2016; Pirard & Hermann, 2015; Borghini & Fumagalli, 2020). However, this last mechanism would require enormous veins/fractures for the slab melts to ascend rapidly and react with the hotter core mantle wedge — where it has been demonstrated that the residual melts at higher temperatures preserve the trace slab-melt composition (Mallik *et al.*, 2015 and 2016). Therefore, another driving-mechanism may occur to explain the survival of slab-melts from the slab-mantle interface to the core mantle wedge.

A time-progressive multi-stage transformation of a pyroxenitic mantle segregation has been inferred from time-series of monogenetic centers in TMVB where erupting magmas become increasingly silica rich with time. This observation has been attributed to a plausible continuous supply of silicic material that repeatedly infiltrates a given parcel of mantle wedge as the slab passes beneath the arc (Straub *et al.*, 2013; Gómez-Tuena *et al.*, 2018b). Then, a sustained infiltration should lead to stronger local SiO_2 enrichment, olivine removal, and the eventual formation of Si-excess pyroxenites. But this hypothesis has not yet been experimentally tested.

Table 1: Starting material compositions used, rock-melt ratio, H_2O content (wt%) for each experiment performed at 3 GPa

Exp.	Starting material		A993	B1110	B1113	A1014	A1021	A1027	D422	B1123	B1130	B54 $^{(6)}$
Ratio$^{(1)}$			50–50	75–25			75–25		50–50			75–25
T (°C)			950	950			800		800			1050
Stage$^{(2)}$			I	I	II	I	II	III	I	II	III	
H_2O (wt%)	10	__	5	7.5	7.5	7.5	7.5	7.5	5	5	5	6
S.M.$^{(3)}$	KLB-1$^{(4)}$	JR-1$^{(5)}$	1	2	3	4	5	6	7	8	9	B1110
			KLB1	KLB1	RES1	KLB1	RES1	RES2	KLB1	RES1	RES2	+ G308
			+ JR1	+ JR-1	+ JR1	+ JR1	+ JR1	+ JR1	+ JR1	+ JR1	+ JR1	
SiO_2	44.8 (2)	76.5 (7)	60.8 (4)	52.8 (2)	58.8 (7)	52.8 (2)	59.3 (5)	58.5 (4)	60.8 (4)	67.6 (4)	69.4 (1)	56.7
TiO_2	0.11 (2)	0.11 (0)	0.11 (1)	0.11 (2)	0.12 (1)	0.11 (2)	0.10 (1)	0.28 (9)	0.11 (1)	0.16 (1)	0.15 (1)	0.2
Al_2O_3	3.51 (5)	13.4 (6)	8.43 (4)	5.97 (4)	7.7(3)	5.97 (4)	8.1 (1)	9.0 (1)	8.43 (4)	10.64 (4)	11.8 (5)	10.1
Cr_2O_3	0.32 (4)	0.01 (0)	0.18 (2)	0.25 (3)	0.18 (2)	0.25 (3)	0.18 (2)	0.3 (1)	0.18 (2)	0.12 (2)	0.10 (4)	0.20
FeO	8.2 (1)	0.77 (2)	4.48 (6)	6.34 (9)	5.0 (5)	6.34 (9)	4.6 (2)	4.4 (1)	4.48 (6)	2.87 (6)	2.5 (3)	4.2
MnO	0.1 (3)	0.12 (0)	0.12 (2)	0.12 (2)	0.13 (2)	0.12 (2)	0.14 (1)	0.19 (1)	0.12 (2)	0.16 (2)	0.23 (4)	0.06
MgO	39.5 (4)	0.13 (0)	19.8 (2)	29.7 (3)	22.8 (1)	29.7 (3)	22.53 (4)	20.5 (3)	19.8 (2)	11.0 (2)	8 (2)	22.4
CaO	3.07 (6)	0.73 (0)	1.90 (3)	2.49 (5)	2.09 (3)	2.49 (5)	2.04 (3)	2.10 (6)	1.90 (3)	1.55 (3)	1.20 (2)	2.7
Na_2O	0.30 (3)	3.7 (8)	2.0 (4)	1.2 (2)	1.5 (2)	1.2 (2)	1.98 (1)	1.7 (2)	2.0 (4)	2.7 (4)	3.1 (4)	0.9
K_2O	0.02 (1)	4.36 (2)	2.18 (1)	1.11 (1)	1.78 (1)	1.11 (1)	1.3 (2)	2.94 (9)	2.18 (1)	3.21 (1)	3.7 (4)	2.3
Total	100	100	100	100	100	100	100	100	100	100	100	100
Mg#	0.89	0.23	0.89	0.89	0.89	0.89	0.90	0.89	0.89	0.87	0.85	0.90

[1] Denotes melt-rock-melt ratio, whereby for example '50–50' refers to mixing of 50 wt% of rock and 50 wt% of new rhyolitic melt.

[2] Denotes consecutive mixing stages (I, II, III) at a given mixing ratio and temperature.

[3] S.M. denotes the bulk starting material. For example, S.M. number 7 is the starting material used for the stage I experiment at 800°C and rock-melt ratio 50 wt% KLB-1 and 50 wt% JR-1, that represent the peridotite rock and the rhyolitic slab partial melt, respectively. The starting material for stage II was calculated from the mixture between the reacted solid residue (RES 1) and fresh JR-1 with same proportions of interaction, 50 wt% and 50 wt% respectively. The same way, stage III was calculated from the mixture of RES 2 and fresh JR-1 at same rock-melt proportions. See Supplementary S.2 for residual composition calculations.

[4] KLB-1 composition and standard deviation as reported in (Davis *et al.*, 2009).

[5] JR-1 has similar composition as reported in (Ando *et al.*, 1989). The number in parentheses of JR-1 indicates standard deviation as $\pm 1\sigma$ obtained from several microprobe analyses. For example, 14.48(9) should be read as 14.48 ± 0.09 wt%. The number in parentheses for the S.M. 1 to S.M. 9 indicates error propagation calculated from the standard deviation of the mixtures KLB-1, JR-1, RES1, and RES2.

[6] This starting material is the mixture of 75 wt% of the solid residue formed at 1050C and 3 GPa (Mallik *et al.*, 2015; experiment G308) and 25 wt% of the rhyolitic melt composition of this study (B1110).

Here, for the first time, we offer an insight into multiple (or 'serial') episodes of rock-melt reaction starting right from the slab-mantle interface and its plausible link with the origin of high-SiO_2 and high-Mg# melts. The repetitive flow of slab additions to a parcel of the mantle wedge at depths of ~90 km (3 GPa) is plausible because (a) at that depth the plate and the mantle wedge are most likely fully-coupled (Syracuse *et al.*, 2010; Abers *et al.*, 2020) and (b) the interaction between silicic slab partial melts and peridotite is so reactive that it can occur at short timescales (within hours at micron scale) compared to the average mantle convection motion or the average plate subduction rate that is in the order of few cm/yr (e.g. Syracuse *et al.*, 2010). To investigate the process of time-progressive peridotite transformation by serial slab additions, we used a simple porous-flow-type experimental setup to simulate multiple additions of fresh silicic slab component to a given parcel of mantle wedge at slab-top conditions (3 GPa and 800–1050°C). Here, we chose a natural rhyolite powder (JR-1) that represents the hydrous slab partial melt component, whose composition is similar to the melts derived from subducted sediments (Hermann & Spandler, 2008) and basaltic slab crust (Rapp & Watson, 1995; Sisson & Kelemen, 2018) at similar slab-top conditions (2.8–4.5 GPa and 700–1050°C). Those rhyolitic slab melts react with an initial fertile and pristine mantle represented by a synthetic lherzolite composition (KLB-1). High proportions of slab component (25 and 50 wt%) were chosen in order to ensure reaction and SiO_2 saturation, and which are consistent with the high proportions (up to 50%) of slab material that were recently inferred for in the erupted andesites of Trans-Mexican Volcanic Belt (Gómez-Tuena *et al.*, 2007; Straub *et al.*, 2015; Parolari *et al.*, 2018, 2021). We use this sequence of experiments to explore how the reacted melts and residues evolve following serial slab additions, and how this may affect the trace elements, in particular the H_2O/K_2O, and H_2O/Ce ratios of slab-melts. A question of interest is whether multiple porous flow reactions may propel slab melts further into the mantle wedge without losing the slab signature. We discuss our experimental results in the context of earlier experimental studies and recent hypotheses on the ascent of melt and buoyant bodies through the mantle wedge either of which be linked to the formation of high-SiO_2 and high-Mg# melts in the sub-arc mantle.

METHODS

Starting materials of serial experiments

The two starting materials consist of a homogeneous mixture of a natural rhyolite powder (JR-1) from Wada-Toge (Nagano, Japan) and a synthetic lherzolite (KLB-1) which were used to represent the silicic slab materials and the sub-arc mantle, respectively. On a volatile-free basis, the synthetic KLB-1 has the same composition as (Davis *et al.*, 2009), and 10 wt% of H_2O was added to this mixture to simulate the hydrous transfer from the slab to wedge. The natural JR-1 sample has a similar composition to (Ando *et al.*, 1989), and the water content (H_2O ~123 ppm) was measured using FTIR (Supplementary data, S.1). Both starting material compositions are given in Table 1.

The experiments were performed in three successive stages to simulate serial addition from the slab. The first stage simulates the initial reaction between the slab material (JR-1) with the peridotite wedge (KLB-1 + H_2O) (Stage I, Eq. 1). It produces a reacted melt (Melt 1) and a mineral assemblage referred to as 'solid residue' (RES 1). Then, the solid residue (RES 1) interacts with a new flux of slab partial melt (JR-1) to produce a second reacted melt (Melt 2) and a solid residue (RES2) (Stage II, Eq. 2). Finally, the solid residue (RES 2) interacts with a fresh slab flux (JR-1) to produce a third melt (Melt 3) and a metasomatic residue (RES 3) (Stage III, Eq. 3). Moreover, to assess the influence of the rock-melt ratio, we performed two different 'sets' of rock-melt ratios. One 'set' used proportions of 75% (by weight) of KLB-1, RES 1, RES 2, and RES 3 each and 25% (by weight) of JR-1. For simplicity we will identify this set of experiment as 75–25 and the rock-melt reaction can be written as follows:

$$\text{Stage I: } KLB-1\ (0.75) + \text{JR-1}\ (0.25) = \text{MELT 1} + \text{RES 1} \quad (1)$$

$$\text{Stage II: } RES1\ (0.75) + \text{JR-1}\ (0.25) = \text{MELT 2} + \text{RES 2} \quad (2)$$

$$\text{Stage III: } RES2\ (0.75) + \text{JR-1}\ (0.25) = \text{MELT 3} + \text{RES 3} \quad (3)$$

The second 'set' represents a larger slab flux with proportions of 50% (by weight) of KLB-1, RES 1, RES 2 or RES 3 each and 50% (by weight) of JR-1. Again, for simplicity, we will refer to this set of experiments as 50–50, and the reactions are the same as Eq. 1, 2, and 3 but substituting the respective proportions. One last experiment represents the infiltration of a reactant melt (MELT 1) that reacts with a preexisting pyroxenite (PX) with proportion of 75–25. This pyroxenite (PX) is the product of a prior reaction between the mantle wedge and slab-melt at 1050°C (from Mallik *et al.*, 2015). The purpose of this last experiment is to see how the residue and melt composition varies at higher temperature. The rock-melt reaction can be written as follows:

$$\text{Stage II: } PX\ (0.75) + \text{MELT 1}\ (0.25) = \text{MELT 2} + \text{RES} \quad (4)$$

The bulk RES was calculated via mass balance from the compositions of the residual minerals (see Supplementary S.2). The bulk RES compositions were synthesized using reagent-grade oxides (SiO_2, TiO_2, Cr_2O_3, FeO, MnO, MgO), carbonates (K_2CO_3, $NaCO_3$, $CaCO_3$), and hydroxides ($Al(OH)_3$), $Mg(OH)_2$). First, the oxides (except FeO) and carbonates were mixed in an agate mortar under ethanol for 45 minutes and air-dried. After this, the mixtures were decarbonated in a Pt crucible in a box furnace. The temperature gradually increased from 400 to 1100°C in approximately 7 hours and was kept at the maximum temperature for 4 hours. Afterward, H_2O (10% by weight) was added in the form of $Mg(OH)_2$ and $Al(OH)_3$, and FeO was also added to the starting material and mixed in the agate mortar under ethanol for 45 minutes and air-dried. The new residue compositions were mixed with their respective proportions of JR-1. The composition of all starting materials used in this study is given in Table 1. All mixtures were stored in a desiccator.

Experimental procedure

Nine experiments were carried out using half-inch assemblies in piston-cylinder devices at the Bayerisches Geoinstitut in Bayreuth (Germany), and one experiment was carried out at the Petrology lab at the University of Arizona. They were performed at 3 GPa and 800 or 950°C, which are relevant to slab-top conditions beneath the arc front in intermediate to warm subduction zones (Syracuse *et al.*, 2010). One last experiment (#B54) has been performed at 1050°C. Here, we explore the effect of *T*, rock-melt ratio, and serial addition of slab-derived partial melt to sub-arc peridotite on the phase equilibria.

Six experiments were conducted at 800°C for 9 days (216 h), simulating all three successive stages (stage I to III) for each mixing ratio of 75–25 and 50–50. At 950°C, 3 experiments were conducted for 7 days (168 h). One experiment was conducted at a 50–50 ratio (Stage I), and the two others were conducted at a 75–25 ratio (Stage I to II). We will identify the individual steps by *T*-X and stage-number, e.g. 800°C/75–25 (stage I) refers to the first stage at 800°C with 75% KLB-1 and 25% JR-1. The experiment at 1050°C was conducted at 75–25 ratio.

A double capsule-design modified from Kägi *et al.* (2005) was used. The inner Au80-Pd20 capsule with 1.6 mm outer diameter was packed with the respective starting material mixtures, welded, and placed inside a 3 mm diameter outer Au80-Pd20 capsule that also contains the same starting material to minimize water and iron loss (Supplementary F.1). To avoid any kind of contamination before packing the starting materials, the capsules were previously cleaned with HCl (20 ml) mixed with deionized water (20 ml) and heated at 150°C for 15 minutes. Afterward, they were cleaned thoroughly with deionized water and dried. The inner and outer capsules were welded using a pulse-arc welder with a tungsten electrode.

To produce crystals sufficiently large for microprobe analysis, all experiments (except A993) were first heated up to 1275°C and kept overnight. The temperature was gradually decreased within 6 hours and kept for 7 to 9 days at 950°C and 800°C, respectively. The temperatures were measured and controlled using a type-S thermocouple (90%Pt/10%Rh–Pt, by weight), with the hot-end of the thermocouple placed above the Al_2O_3 capsule lid (Supplementary F.2). Once the experiments were quenched and decompressed for 20 hours, the capsules were recovered and cut in-to half longitudinally using a wire-saw. Both halves were mounted in epoxy resin, ground with 800-grit silicon-carbide paper, and polished on velvet microcloth with 1 and 3 μm polycrystalline diamond spray.

Scanning electron microscope (SEM)

Energy-Dispersive spetrcoscopy (EDS) analyses and backscattered (BSE) images were done at the Bayerisches Geoinstitut (Germany) and at the Geo Arizona SEM Laboratory (USA) using a Scanning Electron Microscope Leo 1530 Gemini and a Hitachi 3400 N, respectively. The accelerating voltage used was 20 kV with a working distance of 10 mm. Backscattered electron imaging (BSE) was used for texture, grain size, and spatial distribution of the phases. X-ray mapping was used to identify the location of K-rich phases, such as mica, especially in samples where the grain sizes were too small to distinguish phases by visual inspection under high magnification (e.g. sample A993).

Electron microprobe analyses (EMPA)

Major element oxide composition (SiO_2, TiO_2, Al_2O_3, Cr_2O_3, FeO, MnO, MgO, CaO, Na_2O, and K_2O) of the melts and the minerals (pyroxene, quartz/coesite, mica, amphibole, garnet, spinel) were determined by wavelength dispersive analysis using a JEOL JXA-8200 at the Bayerisches Geoinstitut and additional analysis at the Lunar and Planetary Laboratory (USA) using a CAMECA SX100. Operating conditions were 15 kV accelerating voltage and 20 nA beam current with peak counting times of 10s and 5 s on each background for the glasses and peak counting times of 20s and 10s on each background for the minerals. Na in glasses was measured first to prevent its loss during analysis. When possible, a focused beam was used for mineral phases and a defocused beam of 10 μm diameter for glass analysis. To provide a quantitative and representative statistical composition of each phase, 10–20 spots were analyzed. For calibration of the data, the following natural and synthetic reference samples were used: andradite

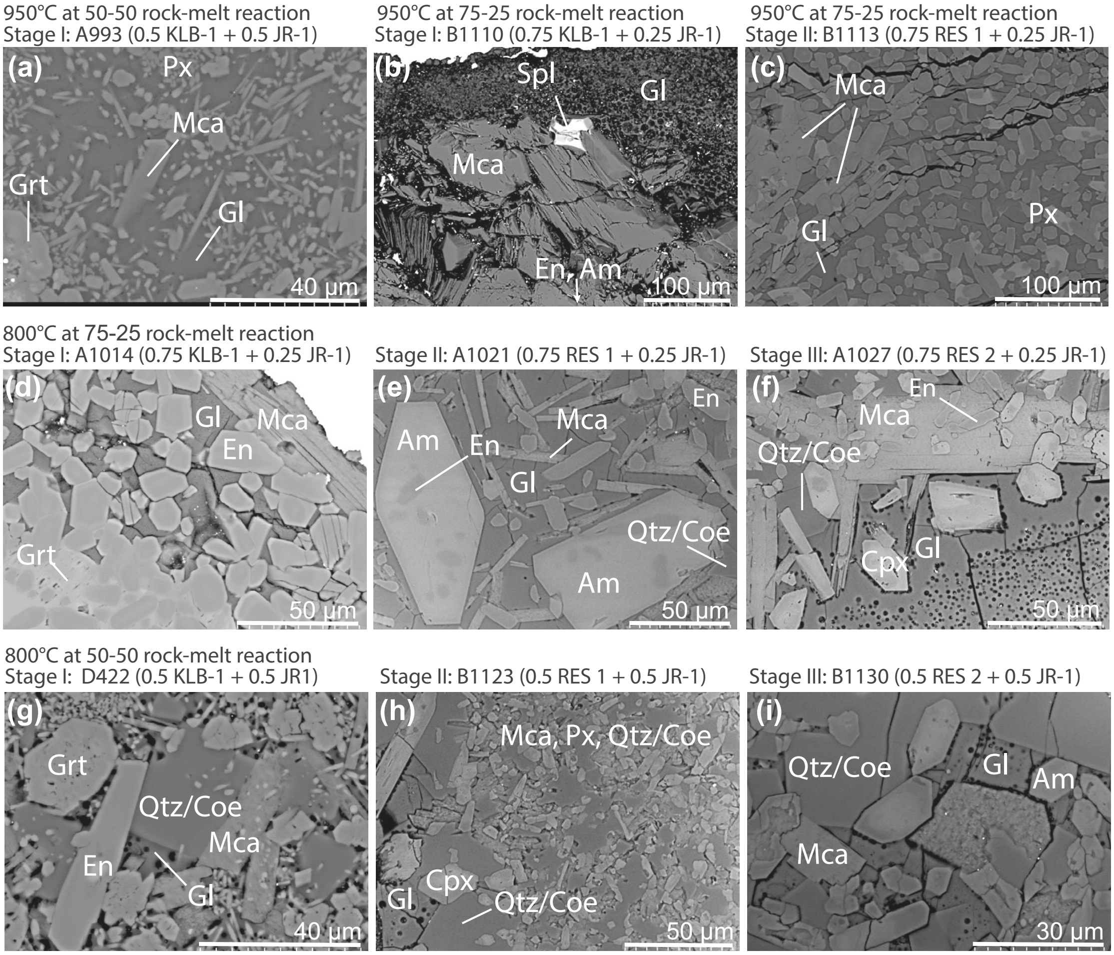

950°C at 50-50 rock-melt reaction
Stage I: A993 (0.5 KLB-1 + 0.5 JR-1)

950°C at 75-25 rock-melt reaction
Stage I: B1110 (0.75 KLB-1 + 0.25 JR-1)

950°C at 75-25 rock-melt reaction
Stage II: B1113 (0.75 RES 1 + 0.25 JR-1)

800°C at 75-25 rock-melt reaction
Stage I: A1014 (0.75 KLB-1 + 0.25 JR-1)

Stage II: A1021 (0.75 RES 1 + 0.25 JR-1)

Stage III: A1027 (0.75 RES 2 + 0.25 JR-1)

800°C at 50-50 rock-melt reaction
Stage I: D422 (0.5 KLB-1 + 0.5 JR1)

Stage II: B1123 (0.5 RES 1 + 0.5 JR-1)

Stage III: B1130 (0.5 RES 2 + 0.5 JR-1)

Fig. 2. SEM photomicrographs of the experimental run products at 3 GPa and 800–950°C. (a–c) are the experiments performed at 950°C, where (a) is at 50–50 ratio and (b) and (c) are consecutive experiments at 75–25 ratio. (d–f) show the serial product of experiments at 800°C and 75–25 ratio, whereas (g–i) show the successive products at 800°C and 50–50 ratio. Notice the small size of the minerals in (a) when no pre-heating (up to 1275°C) is applied. Vesicular texture is commonly observed in melts (e.g. b, f, g, h, i). The cluster of mineral assemblages are represented as general mineral groups (e.g. a and h). Cpx, clinopyroxene; Am, amphibole; En, enstatite; Grt, garnet; Qtz/Coe, quartz/coesite; Mca, mica; Gl, glass; Px, pyroxenes (Cpx + Opx) indicated when the mineral sizes are too small.

(Si, Ca), albite (Na), orthoclase (K, Al), diopside (Si, Ca, Mg), rutile (Ti), Cr_2O_3 (Cr), olivine (Si, Fe), spinel (Al, Mg), pyrope (Si, Al, Mg), and rhodonite (Mn). The last experiment #B54 was analyzed at the Lunar and Planetary Laboratory. Operating conditions were also 15 kV accelerating voltage and 20 nA beam current. Na is measured first to prevent its loss during analysis. A focused beam was used for mineral phases and a defocused beam of 10 μm diameter for glass analysis. For calibration were used: Hakone Anorthite (Al, Ca), Chromite - USNM 117075 (Cr), Rockport Fayalite (Fe), Orthoclase OR-1 (K Si), San Carlos Olivine (Mg), Rhodonite 104 791 (Mn), Crete Albite (Na), Synthetic fluorapatite (P), Natural Rutile (Ti). The chemical composition of the primary and secondary standards are in Supplementary Information (excel).

Experimental results

All experiments show interstitial quench glass and relatively large melt areas close to the outer and inner-capsule walls, along with well-crystallized mineral phases (Fig. 2). The microphotograph of experiment #B54 is found in Supplemental information (F.3). Here, we independently studied the quenched glass representing the reacted melt and the coexistent mineral phases referred to as 'solid residue'. The chemical variation and the proportions of melt and mineral phases (all expressed in weight fractions) are explained in detail hereunder. The melt compositions are normalized to 100% on an anhydrous basis, and the respective compositions and modal proportions of minerals are summarized in Table 2 and Table 3.

Reactant solid residue

The total amount of minerals present ranges from 72 to ~99 wt%, where the percentage is highest in the first stage experiments at a given temperature and decreases with new JR-1 melt addition. None of the experiments contain olivine. Orthopyroxene (44 wt% on average), amphibole (20 wt%), mica (17 wt%), and clinopyroxene (12 wt%) are the four most abundant phases in decreasing order of abundance. However, only mica is present in all the experiments. Ortho- and clinopyroxene are present in most experiments, and amphibole occurs only in those four charges where clinopyroxene is absent or barely detected. Garnet (5 wt%) and spinel (1 wt%) occur only in the first rock-melt reaction. Quartz/coesite (10 wt% on average) is present in five charges. The crystal size ranges from about ~10–50 μm. Only two experiments with exceptionally large crystals of amphibole (stage II) and mica

Table 2: Melt composition (wt%), melt proportion (wt%) and oxygen fugacity for each experiment at 3 GPa

Run No.	**A993**	**B1110**	**B1113**	**A1014**	**A1021**	**A1027**	**D422**	**B1123**	**B1130**	**B54**
Ratio (1)	50–50	75–25			75–25			50–50		75–25
T (°C)	950	950			800			800		1050
S.M. (2)	1	2	3	4	5	6	7	8	9	10
Stage (3)	I	I	II	I	II	III	I	II	III	
Time (h)	168	168	168	216	216	216	216	216	216	120
Capsules	Au	$Au_{80}Pd_{20}$	$Au_{80}Pd_{20}$	$Au_{80}Pd_{20}$	$Au_{80}Pd_{20}$	$Au_{80}Pd_{20}$	$Au_{80}Pd_{20}$	$Au_{80}Pd_{20}$	$Au_{80}Pd_{20}$	$Au_{75}Pd_{25}$
n	3	8	5	4	9	4	1	3	4	4
MELT COMPOSITION										
SiO_2	78 (1)	72.2(5)	72.8 (6)	80(2)	77.3(6)	78.5 (9)	79.1 (0)	78.3(9)	77.4(8)	71 (1)
TiO_2	0.11 (7)	0.11(2)	0.21 (1)	0.11(1)	0.06(2)	0.08 (0)	0.02 (0)	0.04(0)	0.02(1)	0.33 (2)
Al_2O_3	14.7 (3)	18.21(9)	16.7(1)	14.8 (1)	15.4(2)	14.4 (1)	13.2 (0)	15.2(3)	13.8(5)	15.2 (1)
Cr_2O_3	0.02 (3)	b.d.l.**(4)**	b.d.l.	0.01(1)	b.d.l.	0.01(1)	0.01 (0)	b.d.l.	0.01(1)	0.02 (0)
FeO	1.0 (3)	1.6(1)	0.7 (1)	0.67 (4)	0.54(5)	0.47 (1)	0.57 (0)	0.44(3)	0.48(6)	1.0 (1)
MnO	0.03 (2)	0.04(1)	0.05 (1)	0.02(1)	0.02(1)	0.04 (1)	0.06 (0)	0.07(1)	0.08(2)	0.01 (1)
MgO	3.8 (9)	0.6(1)	1.4 (3)	0.94 (3)	0.47(3)	0.34 (3)	3.45 (0)	0.33(6)	0.4(1)	1.8 (4)
CaO	0.77 (6)	2.21(9)	2.08 (3)	0.77 (2)	1.03(4)	1.04 (3)	0.57 (0)	0.49(1)	0.34(3)	2.8 (1)
Na_2O	0.47 (7)	1.3(2)	2.1 (2)	1.4 (1)	2.8(4)	2.5 (6)	1.55 (0)	2.31(1)	2.6(3)	2.27 (7)
K_2O	1.1 (1)	3.8(3)	4.1 (1)	1.14 (2)	2.3(3)	2.6 (4)	1.40 (0)	2.9(1)	4.9(3)	5.9 (2)
Total	100	100	100	100	100	100	100	100	100	100
Tot. (Hydro)(5)	85 (1)	65.5 (5)	87.5 (4)	75.6 (0)	85.5 (7)	86.3 (5)	87 (0)	87.5 (1)	78.5 (7)	89.5 (6)
Mg# (6)	0.87 (0.1)	0.40 (5)	0.79 (13)	0.71 (2)	0.61 (3)	0.56 (4)	0.91 (1)	0.57 (7)	0.61 (3)	0.75 (2)
Melt (wt%)	28 (0)	2 (0)	24 (1)	+ **(7)**	28 (1)	23 (2)	11 (1)	16 (3)	18 (5)	27 (1)
ρ_{Hydro} (8)	2.6 (1)	2.17 (3)	2.64 (5)	2.45 (2)	2.65 (1)	2.66 (6)	2.67 (0)	2.70 (4)	2.53 (2)	2.8f (1)
$\rho_{Non\text{-}hydro}$ (9)	2.99 (2)	3.04 (0)	3.03 (0)	2.97 (0)	3 (0)	2.99 (1)	2.98 (0)	2.99 (0)	3.02 (3)	3.07 (2)
ΔfO_2 QFM(10)	—	−2.30 (3)	−4.33 (3)	−4.4 (3)	−2.4 (3)	−3.0 (3)	−3.4 (3)	−3.0 (3)	−3.6 (3)	—
ΔfO_2 NNO	—	−2.02 (3)	−4.05 (3)	−4 (3)	−2.0 (3)	−2.5(3)	−3.0 (3)	−2.6 (3)	−3.2 (2)	—

[1] Denotes rock-melt ratio investigated, whereby for example 50–50 indicates 50 wt% of rock and 50 wt% of fresh rhyolitic melt (JR-1).

[2] S.M. indicates the bulk starting material used for each experiment. The chemical composition is found in Table 1. For example, S.M. number 4 is the starting material used for the stage I experiment at 800°C and rock-melt ratio 75 wt% KLB-1 and 25 wt% JR-1, that represent the peridotite rock and the rhyolitic slab partial melt, respectively. The starting material for stage II was calculated from the mixture between the solid residue (RES 1) and fresh JR-1 with same proportions of interaction, 75 wt% and 25 wt% respectively. The same procedure for stage III. The residual composition (RES) calculations can be found in Supplementary S.2.

[3] Denotes the stage of rock-melt interaction for a given temperature and mixing ratios.

[4] b.d.l denotes below detection limit. The number in parentheses indicates standard deviation as ±1σ obtained from several microprobe analyses. For example, 14.48(9) should be read as 14.48 ± 0.09 wt%.

[5] Non-normalized total, reflecting the hydrous nature of the melts.

[6] Mg# = [molar ratio of MgO/(MgO+ molar FeO]. The iron is considered as total FeO. The error propagation for Mg# in parentheses. For example, 0.79 (13) as 0.79 ± 0.13.

[7] (+) denotes the trace presence of the mineral (observable), but not detected by mass balance.

[8] Density of the experimental melts expressed as g/cm^3 (hydrous conditions). [9] Density of the experimental melts expressed as g/cm^3 (anhydrous conditions).

[10] The difference between the oxygen fugacity estimated by Barr & Grove, (2010) and FMQ (fayalite-magnetite-quartz) buffer of O'Neill & wall, (1987) and Ballhaus *et al.* (1991).

(stage III) were found at the 'set' 800°C/75–25 with a size of ~50–200 μm.

There is an overall trend in residuum development. Regardless of variable temperature (800°C or 950°C) or rock-melt ratio (75–25 or 50–50), in all experiments the peridotite lithology is completely transformed to a mica-rich pyroxenite lithology ± amphibole ± quartz/coesite ± garnet/Spinel. The transformation progresses with increasing slab addition (stage I through III) where orthopyroxene is being drastically depleted and clinopyroxene and mica became predominant. It is also observed that the larger the slab-partial melt influx, the faster the transformation with a substantial increase of quartz/coesite (up to 26 wt%). Also is observed that the bulk composition - in both rock-melt ratio series - of the metasomatized solid residue is eventually enriched in SiO_2, Al_2O_3, Na_2O, and K_2O (provided by JR-1) with a corresponding depletion of MgO, FeO, CaO given the lack of fresh peridotite addition, whereas the Mg# remains fairly constant (86–93). Rock-melt reactions at 800–1050°C form mineral heterogeneities within species (e.g. clinopyroxene, mica) that are a product of miscibility gaps. Such observation is addressed below.

The bulk residue composition and the proportions of each phase group (e.g. orthopyroxene, clinopyroxene, mica, amphibole, garnet) are given in Table 3, and the individual mineral composition used in the mass balance are in Supplementary Table 1 to 6.

Orthopyroxene

Orthopyroxene is the dominant solid phase (33–69 wt%) in all experiments, except for the experiments at 800°C/50–50 series, where it is present only in trace amounts in stage II and absent in stage III. Hotter slab-top conditions (950°C) and a lower slab flux (75–25) seem to favor the formation of homogeneous orthopyroxene from stage I to II (~2 wt% Al_2O_3, ~4.5 wt% FeO) whereas at higher slab influx (50–50), orthopyroxene is enriched in Al_2O_3 (~17 wt%) and FeO (7.5 wt%).

Interestingly, at 800°C and lower slab flux (75–25), the proportion of orthopyroxene decreases from 69 to 44 wt% from stages I through III with almost invariant composition(56.6–55.5 wt% SiO_2, ~5 wt% FeO, 35–33 wt% MgO, 1.7–2.6 wt% Al_2O_3). However, higher slab flux (50–50) leads to significant reduction of orthopyroxene

Table 3: Bulk solid residue composition (wt%), solid phase proportions (wt%) in each experiment at 3 GPa

Run No.	**A993**	**B1110**	**B1113**	**A1014**	**A1021**	**A1027**	**D422**	**B1123**	**B1130**	**B54**
Ratio (1)	50–50	75–25		75–25			50–50			75–25
T (°C)	950	950		800			800			1050
S.M. (2)	1	2	3	4	5	6	7	8	9	10
Stage (3)	I	I	II	I	II	III	I	II	III	
Time (h)	168	168	168	216	216	216	216	216	216	120
Capsules	Au	$Au_{80}Pd_{20}$	$Au_{80}Pd_{20}$	$Au_{80}Pd_{20}$	$Au_{80}Pd_{20}$	$Au_{80}Pd_{20}$	$Au_{80}Pd_{20}$	$Au_{80}Pd_{20}$	$Au_{80}Pd_{20}$	$Au_{75}Pd_{25}$
RESIDUE COMPOSITION										
SiO_2	54 (1)	53 (1)	56 (5)	53.6 (6)	51.7 (5)	52.8 (8)	58.5 (1)	62 (3)	68.6 (1)	52.0 (1)
TiO_2	0.33 (4)	0.12 (1)	0.16 (1)	0.10 (2)	0.4 (1)	0.3 (1)	0.21 (4)	0.2 (0)	0.20 (2)	0.24 (3)
Al_2O_3	6.9 (7)	5.8 (4)	5.0 (1)	6.3 (2)	7.91 (5)	7.7 (2)	7.80 (8)	10.2 (9)	11.45(9)	8.36 (4)
Cr_2O_3	0.18 (9)	0.24 (3)	0.22 (2)	0.24 (2)	0.35 (7)	0.47 (8)	0.22 (6)	0.19 (1)	0.16 (0)	0.24 (6)
FeO	7.4 (6)	6.5 (7)	3.9 (5)	5.9 (3)	6.1 (2)	5.7 (1)	5.00 (5)	4.2 (6)	2.4 (2)	5.1 (3)
MnO	0.27 (4)	0.12 (3)	0.19 (1)	0.15 (1)	0.21 (1)	0.28 (2)	0.19 (1)	0.34 (1)	0.26 (1)	0.05 (2)
MgO	25.7 (3)	30.3 (2)	30.3 (2)	30.00 (5)	26.54 (0)	26.58 (2)	21.9 (2)	15 (3)	8.9 (6)	30.0 (4)
CaO	2.1 (2)	2.56 (4)	2.33 (6)	2.4 (1)	2.95 (3)	2.5 (1)	2.4 (3)	1.6 (0)	1.34 (5)	2.8 (5)
Na_2O	0.93(2)	0.76 (3)	0.63 (5)	0.50 (8)	0.64 (5)	0.8 (1)	1.68 (2)	2.5 (3)	3.3 (3)	0.18 (5)
K_2O	2.4 (2)	0.96 (1)	1.23 (5)	0.77 (2)	3.17 (2)	2.7 (1)	2.05 (7)	3 (0)	3.4 (2)	0.9 (1)
Total	100	100	100	100	100	100	100	100	100	100
Residue (wt%) (4)										
Opx	46 (2)	68 (0)	57 (1)	67 (1)	33 (2)	44 (2)	41 (3)	+	—	47 (1)
Cpx	1 (0)	+	11 (1)	10 (1)	+	11 (1)	18 (2)	41 (10)	—	4 (2)
Am	11 (0)	24 (0)	—	—	20 (2)	—	—	—	26 (3)	—
Mca	13 (2)	5 (0)	7 (1)	8 (0)	19 (1)	21 (2)	20 (2)	26 (1)	30 (5)	6 (1)
Ti-Mag	—	1 (0)	—	—	—	—	—	—	—	—
Grt	+	—	—	14 (2)	—	—	+	—	—	16 (0)
Qtz/Coe	—	—	—	—	+	+	8 (2)	17 (1)	26 (3)	—
ρ_{BK} (5)	3196 (22)	3316 (18)	3290 (16)	3385 (7)	3180 (12)	3215 (26)	3187 (23)	3062 (19)	2943 (11)	3402 (4)
Mg# (6)	0.86 (0.1)	0.89 (0.1)	0.93 (6)	0.90 (0.1)	0.89 (0.1)	0.89 (0.1)	0.89 (0.1)	0.87 (0.1)	0.87 (0.1)	0.91 (0)
$\sum r^2$ (7)	3 (2)	0.15 (0)	4 (1)	0.94 (3)	0.9 (1)	0.4 (2)	0.22 (0)	0.85 (2)	0.08 (1)	0.07 (5)
Fe_{loss} % (8)	0	0.1	39 (7)	9 (0)	7 (2)	5 (1)	0.3	28	11	4 (3)

[1] Denotes melt-rock ratio investigated, whereby for example 75–25 indicates 75 wt% of rock and 25 wt% of fresh rhyolitic melt.

[2] S.M. indicates the starting material composition used for each experiment (bulk composition). The chemical composition is showed in Table 1. For example, S.M.C number 4 is the starting material used for the stage I experiment at 800 °C and rock-melt ratio 75 wt% KLB-1 and 25 wt% JR-1, that represent the peridotite rock and the rhyolitic slab partial melt, respectively. The starting material for stage II was calculated from the mixture between the solid residue (RES 1) and fresh JR-1 with same proportions of interaction, 75 wt% and 25 wt%, respectively. The same way, stage III was calculated from the mixture of RES 2 and fresh JR-1 at same rock-melt proportions. The residual composition calculations can be found in Supplementary S.2.

[3] Denotes the stage of rock-melt interactions for a given temperature and mixing ratios.

[4] Number denotes phase proportions in wt% in the residues. The plus sign (+) denotes the trace presence of the mineral (observable), but not detected by mass balance. The large minus sign (—) denotes the absence of the mineral from the system. The general groups (Opx, Cpx, Mca, Mca, Grt . . .) are the sum of all different species observed in each experiment and detected by mass. Each individual mineral phase composition is disclosed in Supplementary Table 1–6. Abbreviations: Opx, orthopyroxene; Cpx, clinopyroxene; Am, amphibole; Bt, biotite; Ti-Mag, Titanium-magnetite; Grt, garnet; Qtz/Coe, quartz-coesite.

[5] Bulk rock density expressed in kg/m^3 (See Supplementary S.4).

[6] Mg# = [molar ratio of MgO/(MgO+ molar FeO]. The iron is considered as total FeO. The error propagation for Mg# is indicated in parentheses. For example, 0.93 (6) as 0.93 ± 0.6.

[7] Sum of squared residuals obtained from mass balance of components on a water-free basis (see Supplementary S.2).

[8] Fe loss % (relative) = [Fe bulk starting material - Fe calculated from mass balance/ Fe bulk starting material] × 100.

proportion from stage I (~40 wt%) until it is a trace in stage III. The MgO content (33 to 31 wt%) decreases and an increase of Al_2O_3 (3 to 3.4 wt%) and FeO (6 to 7 wt%). At 1050°C (#B54), enstatite show similar composition as the enstatites formed at stage I at 800–950°C. With high Mg# numbers of 88–93, the orthopyroxene is enstatitic. The mineral composition and the structural formulae are listed in Supplementary Table 1.

Amphibole

Amphiboles occur abundantly in only four experiments. In hotter slab-top conditions (950°C), amphibole is stable only in stage I at both rock-melt ratios. At the lower slab flux (75–25) the proportion of amphibole is ~24 wt% and are enriched in FeO (~9 wt%) and CaO (~9 wt%). However, at the higher slab flux (50–50), the proportion of amphibole is reduced almost by half (11 wt%) at similar FeO (~9 wt%) and slightly higher in CaO (~11 wt%).

In intermediate conditions (800°C), amphibole only appears in stage II in the 75–25 series and in stage III in the 50–50 series. At lower slab flux (75–25), the proportion of amphibole is ~20 wt% and is characterized by FeO (~6 wt%) and CaO (~8 wt%). At higher slab flux (50–50) and stage III, four different compositional amphiboles are formed (~26 wt% total abundance), of which two are determined to be Eckermannite and magnesio-cummingtonite and two other amphiboles rich in Na (~8 wt% Na_2O and 5 wt% CaO) and Ca (~8 wt% CaO). The amphiboles formed in the 50–50 experiments are significantly smaller (10–50 μm) than the 75–25 experiments (50–200 μm). The Mg# of the amphiboles varies from 69 to 88. The composition and the structural formulae are listed in Supplementary Table 2. The mineral compositions were recalculated to an anhydrous formula unit containing 23 O atoms, assuming all Fe as Fe^{2+}.

Mica

Mica is present in all experiments as an aggregate of bladed crystals that are significantly smaller (5–20 μm) in the 50–50 experiments relative to the 75–25 experiments (20–200 μm). Their proportion increases with increasing slab flux and lower temperatures. At hotter slab-top conditions (950°C) and lower slab flux (75–25), mica proportion increase from 5 to 7 wt% from stage I to II.. At the same temperature but higher slab flux (50–50), the proportion of mica increases to 13 wt% (Stage I). In both scenarios, the composition of mica does not vary significantly. Still, mica shows a slight K_2O increase (8.7 to 9.1 wt%) and decrease of FeO (7–2 wt%) at 950°C/75–25 from stage I to II.

At intermediate conditions (800°C) and lower slab flux (75–25), mica proportions increase from 8 to 21 wt% from stage I through III, and their composition show an increase of SiO_2 (~40 to 43 wt%), K_2O (8.6 to 9.3 wt%), Al_2O_3 (~14 to 17wt%), FeO (~4 to 5 wt%). In contrast, MgO decreases (~24 to 19 wt%). At higher slab flux (50–50), mica becomes the dominant phase with proportions that increase from 20 to 30 wt% from stage I to III. This increase is again coupled with a similar compositional trend, such as an increase of SiO_2 (~45 to 53 wt%), K_2O (~8 to 11 wt%), Al_2O_3 (~16 to 24 wt%), a relatively constant FeO (~4 wt%), and a drastic decrease of MgO (~20 to 6 wt%). Overall, mica has a chemical formula, based on 11 O atom, of $[K_{0.81}\ Na_{0.06}]_{0.87}[Mg_{1.99}\ Fe_{0.26}\ Al_{0.46}\ Ti_{0.03}]_{\Sigma 2.75}\ [Al_{0.91(0)}\ Si_{3.09(0)}]_4\ O_{10}\ (OH)_2$. At higher temperatures (1050°C, #B54) the mica is phlogopite in composition. The composition of micas and their respective structural formulae and proportions (wt%) are summarized in the Supplementary Table 3.

Clinopyroxenes

Grains of omphacite, augite, diopside, and rarely pigeonite are present in all the experiments except for stage III of 800°C/50–50. The abundance of the clinopyroxene seems to be positively correlated with the continuous addition of fresh slab partial melt, lower temperatures (800°C) and, the disappearance of amphiboles — clinopyroxenes tend to disappear when amphiboles are present. The composition of the clinopyroxene reflects the successive addition of fresh alkali-rich rhyolitic slab melt, showing a trend from Ca-rich clinopyroxenes (diopside, omphacite) toward alkali-rich clinopyroxenes from stage I through III.

At hotter slab-top conditions (950°C) and lower slab flux (75–25), the proportions of clinopyroxene increase from stage I to II (trace amounts to 11 wt%, respectively). K_2O-depleted augite is formed in stage I, while at stage II there are different compositional types of clinopyroxenes, which are Al-omphacites and omphacite rich in K_2O (~1.7 wt%). At the same temperature (950°C) but higher slab flux (50–50) and stage I, also produces omphacites that are more FeO (~6 wt%), Na_2O (~5 wt%) and Al_2O_3-rich (~9 wt%) compared to the omphacites formed at lower slab flux (75–25). At higher temperatures (1050°C, #B54) the clinopyroxene is diopside.

At intermediate slab-top conditions (800°C) and lower slab flux (75–25), the clinopyroxene proportions decrease from stage I to II (from ~10 wt% to trace) but increase from stage II to III (to ~11 wt%). In stage I, the clinopyroxenes are diopside (CaO, ~18 wt%) and Na-Al-omphacite (~16 wt% Al_2O_3 and ~9 wt% Na_2O). In stage II, only a trace of Fe-rich diopside is detected (~16 wt% CaO and ~8 wt% FeO) along with big crystals of amphiboles. In stage III, with more slab melt addition, the omphacites display lower CaO (~13 wt%), FeO (~6 wt%), and Na_2O (~5 wt%). At the same temperature (800°C) and higher slab flux (50–50), clinopyroxenes appear only in stage I (~18%) and II (~41%) but are absent in stage III when amphibole is present. The composition of the clinopyroxenes is also variable. In stage I, three types of omphacites, which one is Na-Al-omphacite (~13 wt% Al_2O_3, ~7 wt% Na_2O). In stage II, Na-Al-omphacite and Al-pigeonite are formed. Overall, omphacite are found in all experiments, but augite and pigeonite is only found at 950C/75–25 (stage I) and 800°C/50–50 (stage II), respectively. The Mg# of the clinopyroxenes ranges from 71 to 95. The proportions and chemical composition of all clinopyroxenes detected by mass balance and the respective structural formulae are found in Supplementary Table 4.

Silica phase (quartz/Coesite)

Microcrystalline and euhedral silica phase is present only at lower temperatures (800°C), and their proportions are positively correlated with the slab flux. For example, at 800°C and low slab flux (75–25), is absent in stage I and increases to 1 wt% from stages II to III, whereas at high slab flux (50–50), the proportions increase from ~8 to 26 wt%. The silica phase could be either quartz or coesite, as the experimental *P–T* conditions (950°C and 800°C at 3 GPa) are very close to the quartz-coesite transition (e.g. Bose & Ganguly, 1995). Here we used thermodynamic properties from Holland & Powell (1990) to determine the transition. Both silica phases formed at 3 GPa and 800–950°C should be in the coesite stability field. However, there are discrepancies in the literature when determining the quartz-coesite transition (See Supplementary S.3). We increased the *T* to 1275°C where quartz is stable and cooled down to the target *T* (800–950°C) where coesite may be stable. The kinetics of quartz-coesite transformation can be slow (Perrillat *et al.,* 2003) and quartz can remain as a metastable phase. Therefore, we decided to label this phase as quartz/coesite and neither of the two silica phases affect the main results of this study. The chemical formula of the silica phases was determined based on 2 O atoms, and have trace amounts of FeO, Al_2O_3, and K_2O. The composition, structural formulae and proportions (wt%) are summarized in the Supplementary Table 5.

Garnet

At hotter slab-top conditions (950°C) and high slab flux (50–50, stage I), the small euhedral crystals of garnet (7 μm) show a distinctive core and rim. The composition was measured at the rim, where garnets are rich in FeO (~11 wt%) and CaO (~4 wt%). At intermediate temperature (800°C), garnet is present only in stage I of both rock-melt ratios (75–25 and 50–50). These garnets have small inclusions of homogenous orthopyroxenes. At lower slab flux (75–25), a few large crystals (≥100 μm) are formed with a total modal proportion of ~14 wt%. They are rich in FeO (~14 wt%) and CaO (~6 wt%). At higher slab flux (50–50) the garnet has less FeO (~9 wt%) and CaO (~5 wt%) and smaller sizes (10–35 μm). At high temperature (1050°C, #B54) garnet is also abundantly present (16.6 wt%). The averaged chemical formula of the garnets, determined based on 12 O atoms, is $[Fe_{0.68(2)}\ Ca_{0.36(2)}\ Mg_{1.98(2)}\ Mn_{0.04(1)}]_{3.06}\ [Al_{1.96(1)}\ Cr_{0.01(0)}\ Ti_{0.02(0)}]_{1.99}\ [Si_{2.97(2)}]\ O_{12}$. Therefore, the garnets are considered as Fe rich-pyrope. The composition and structural formulae are given in Supplementary Table 6.

Titanium-magnetite

A single crystal of Ti-magnetite is present only at 950°C (stage I) and low slab flux (75–25). It is composed of TiO_2 (~7 wt%) and FeO (76.61 wt%) with trace amounts of Al_2O_3 (2.95 wt%), Cr_2O_3 (0.70 wt%) and MgO (1.02 wt%). On the basis of 4 O atoms, the chemical formula is $[Fe_{3.09(2)}\ Ti_{0.27(0)}]\ O_4$. The composition is given in Supplementary Table 6.

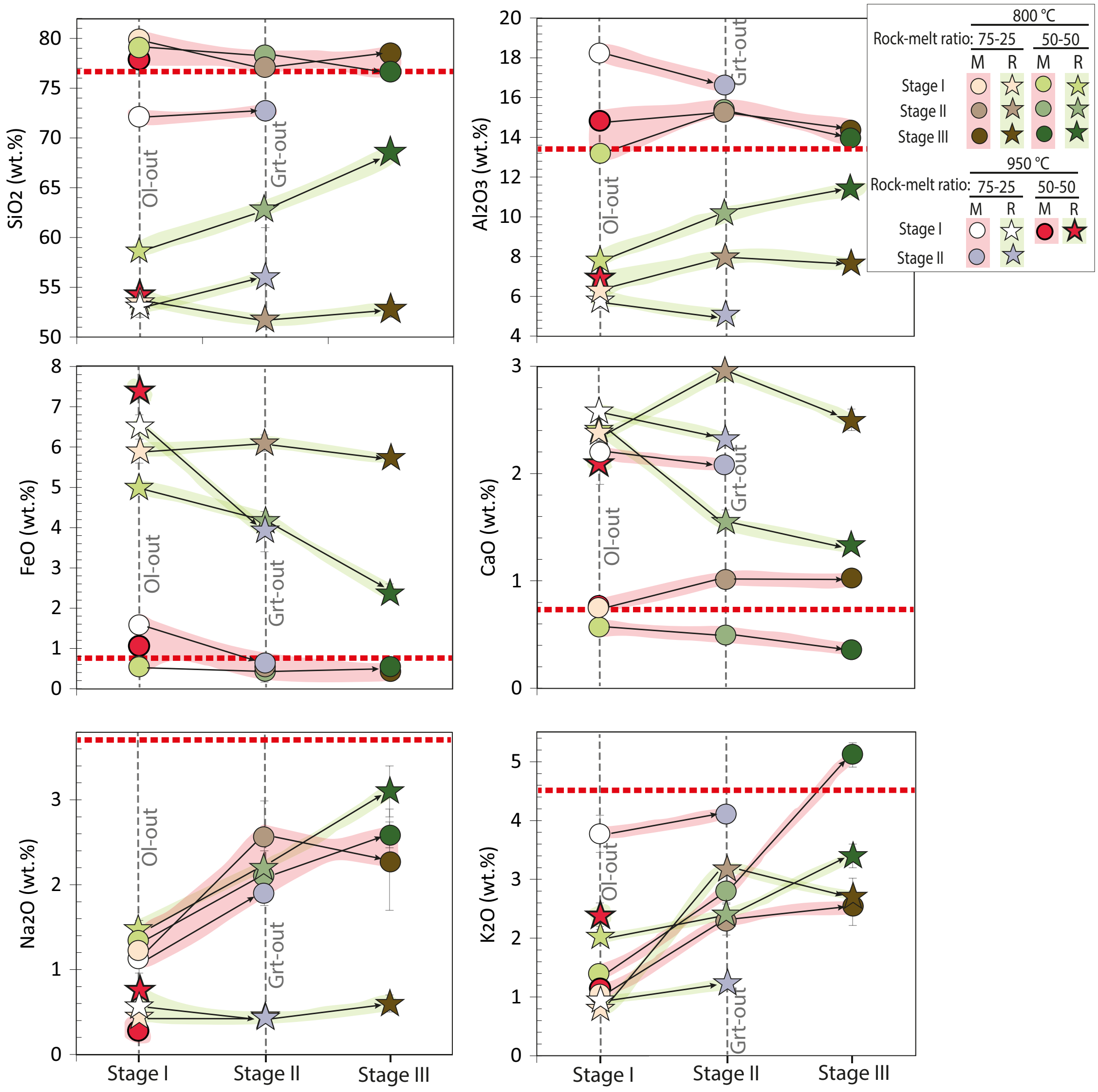

Fig. 3. Major oxide elements diagrams for the nine experiments performed at 3 GPa. The melts are on a free water basis. Red-dashed horizontal line corresponds to the oxide concentration of the pristine silicic slab partial melt composition (JR-1). M, melt (circle symbol); R, residue (star symbol). The bulk residue reflects the compositional features of the melt with which is equilibrated at the respective stage. Both melts and residue show a tendency to resemble the slab-melt compositions (JR-1). The error bars are smaller than the symbol sizes for certain data points. Olivine is not present in this study right from stage I, and Garnet is not stable after a second slab flux, as indicated by the vertical dashed lines.

REACTANT MELTS

The melt occurs interstitially and contains spherical vesicles, which is consistent with the low total sum of oxides (85–87 wt%) and indicates volatile-rich, and partially degassed melts (Fig. 2, d). The melt proportion (expressed in weight fractions) increases with increasing slab flux and temperature. For example, at hotter slab-top conditions (950°C) and lower slab flux (75–25), the melt proportion increases from 2 to ~24 wt%, whereas at the same temperature but higher slab flux (50–50), the melt proportion is ~28 wt%. At intermediate temperatures (800°C), the melt proportions at the lower slab flux (75–25) increase up to ~23 wt%, whereas at the higher slab flux (50–50), the melt proportions increase from 11 to 18 wt%. The proportions of melt in each experiment are found in Table 2.

On a water-free basis, all experimental melts are dacitic to rhyolitic in composition (72–80 wt% SiO_2) and display a general increase of alkalis (K_2O and Na_2O) and decrease of FeO, MgO, and CaO as a function of the increasing slab flux. The reacted melts have 79 to 97% more MgO (~0.3 to 3.8 wt%) than the original JR-1 (0.13 wt%). In contrast, FeO in the reacted melts (~0.5 to 1.6 wt%) can be both higher (up to ~70%) or lower than in JR-1 (0.77 wt%). Therefore, the reacted melt's Mg# (40–91) is higher than JR-1 (Mg# =24). However, the Mg# tends to decrease progressively from stages I through III, which correlates with the notable decrease of MgO content in the melts (by ~93%, average) relative to the lesser decrease of FeO (by ~26%, average). Likewise, CaO is gradually depleted (~2 to 0.3 wt%), and Al_2O_3 is variable (~13 to 18 wt%) relative to JR-1 (~0.7 wt% CaO and ~13.5 wt% Al_2O_3). The effect of the increasing slab flux is to be thus best documented by the least compatible elements, K_2O and Na_2O, which both increase with increasing slab flux (~1.8 to 8 wt% alkalis). Overall, despite the fluctuations induced by sequestration into minerals, the reacted melt compositions converge toward JR-1 in composition with successive addition of slab flux (Fig. 3). The larger the slab flux, the faster (fewer stages) is the convergence toward JR-1 composition.

At hotter slab-top conditions (950°C) and lower slab flux (75–25) from Stages I to II, the melts increase in Na_2O (~1 to 2 wt%), are relatively constant in MgO (~1 wt%), Al_2O_3 (~17.5 wt%) K_2O (~4 wt%), CaO (~2 wt%) and SiO_2 (~72 wt%) and decrease in FeO (~2 to 1 wt%). The Mg# increases from 40 to 79. At the same temperature (950°C) but with higher slab flux (50–50), the rhyolitic melt displays a higher MgO (~4 wt%) and FeO (~1 wt%), giving an Mg# of 87. However, Al_2O_3 (~15 wt%), CaO (~0.8 wt%), Na_2O (~0.5 wt%), and K_2O (~1 wt%) are low.

At intermediate subduction zone (800°C) and lower slab flux (75–25) and from stage I to III, the melts decrease in SiO_2 (~80 to 78 wt%), MgO (~1 to 0.3 wt%) and FeO (~0.7 to 0.5 wt%), and substantially increase in K_2O (~1 to 3 wt%) and Na_2O (~1 to 3 wt%) while they keep relatively constant CaO (~1 wt%) and Al_2O_3 (~14.8 wt%). The Mg# decreases from 71 to 56. At the same temperature (800°C) but higher slab flux (50–50) from stages I to III, the melts decrease in SiO_2 (~79 to 77 wt%), MgO (~3.5 to 0.4 wt%), FeO (~0.6 to 0.5 wt%), and CaO (~0.6 to 0.3 wt%), while K_2O (~1 to 5 wt%) and Na_2O (~1 to 3 wt%) increase. The Al_2O_3 remains relatively constant at values between 13 and 15 wt%. The Mg# decreases from 91 to 61. All reacted melts at 800°C are modally quartz/coesite-saturated (quartz/coesite present in the liquidus).

MELTING REACTIONS OF SUCCESSIVE ADDITIONS OF RHYOLITIC SLAB FLUX AT 3GPA

We calculate the following melting reactions (normalized to 1 g of melt) in each experiment by mass balance to study the solid phases that contribute to melt formation or consumption with changes of T, P, and H_2O content (for details about constructing melting reactions see Supplementary S.4). The minerals in the equation like olivine, orthopyroxene, clinopyroxene, mica, amphibole, garnet/spinel, and quartz/coesite are abbreviated as Ol, Cpx, Mca, Am. Grt/Spl, Qtz/Coe, respectively.

The initial melting reaction produced at hot slab-top condition (950°C) and higher slab flux (50–50) will consumed melt to produce an olivine-free assemblage consisting of orthopyroxene, amphibole, and mica:

$$\mathit{Stage\ I}: 1.41\,\mathit{Ol} + 0.23\,\mathit{Grt} + 0.23\,\mathit{Cpx} + 1\,\mathit{melt} = 1.86\,\mathit{Opx} + 0.50\,\mathit{Am} + 0.59\,\mathit{Mca} \tag{5}$$

The same temperature (950°C) but lower melt flux (75–25) produces an olivine-free assemblage that consists of orthopyroxene + amphibole + mica + titanium-magnetite formed at the expense of olivine, garnet, clinopyroxene, and melt (Eq. 6, Stage I). During a second influx of slab partial melt (Eq. 7, Stage II), amphibole is completely exhausted to form orthopyroxene +clinopyroxene + mica. Note that garnet is completely consumed and does not reappear in Stage II.

$$\mathit{Stage\ I}: 2.00\,\mathit{Ol} + 0.39 + \mathit{Grt} + 0.39\,\mathit{Cpx} + 1.00\,\mathit{melt} = 2.5\,\mathit{Opx} + 1.04\,\mathit{Am} + 0.2\,\mathit{Mca} + 0.04\,\mathit{Ti\text{-}Mag} \tag{6}$$

$$\mathit{Stage\ II}: 22.40\,\mathit{Am} + 1.00\,\mathit{melt} + 1.20\,\mathit{Spl} = 14.00\mathit{Cpx} + 6.60\,\mathit{Opx} + 4.00\,\mathit{Mca} \tag{7}$$

Olivine-free lithologies are also created at intermediate slab-top conditions (800°C) at 75–25 rock-melt ratios. In Stage I, the melt is consumed and produces a mica- and garnet-bearing pyroxenite (Eq. 8). The addition of a second influx (Stage II) produces melt due to enhanced fertility of the bulk composition and the excess of alkalis that cannot be hosted by amphibole and mica alone (Eq. 9). In Stage III, amphibole and melt are consumed to produce orthopyroxene + clinopyroxene + mica (Eq. 10). The influx of alkali and alumina-rich rhyolitic melts forms abundant mica and the eventual saturation of quartz/coesite (Stages II through III). The behavior of orthopyroxene varies through the stages of rock-melt reaction. While orthopyroxene is produced in stage I, it is consumed in stage II and again produced in stage III by melt consumption. Garnet is completely consumed and is no longer present in stages II and III.

$$\mathit{Stage\ I}: 1.84\,\mathit{Ol}{+}0.04\,\mathit{Spl}{+}1.00\,\mathit{melt} = 2.36\,\mathit{Opx}{+}0.32\,\mathit{Mca}{+}0.20{+}\mathit{Grt} \tag{8}$$

$$\mathit{Stage\ II}:\ 6.33\,\mathit{Opx} + 2.00\,\mathit{Cpx} + 3.33\,\mathit{Grt} = 6.33\,\mathit{Am} + 4.00\,\mathit{Mca} + 0.33\,\mathrm{Qtz/Coe} + 1.00\,\mathit{Melt} \tag{9}$$

$$\mathit{Stage\ III}:\ 10.00\,\mathit{Am}{+}1.00\,\mathit{melt} = 5.00\,\mathit{Opx}{+}5.00\,\mathit{Cpx}{+}1.00\,\mathit{Mca} \tag{10}$$

Equations (11)–(13) show the melting reactions produced at intermediate slab-top condition (800°C) and at higher slab flux (50–50). At these conditions, the wedge peridotite is transformed to a quartz/coesite-bearing mica-rich pyroxenite. The proportion of quartz/coesite increases from stages I through III, and thus, the melts are quartz/coesite-saturated. Garnet is consumed and is not produced after the first rock-melt reaction.

$$\mathit{Stage\ I}:\ 0.79\,\mathit{Ol} + 0.13\,\mathit{Grt} + 1.00\,\mathit{melt} = 0.74\,\mathit{Opx} + 0.46\,\mathit{Cpx} + 0.51\,\mathit{Mca} + 0.20\,\mathrm{Qtz/Coe} \tag{11}$$

$$\mathit{Stage\ II}:\ 0.56\,\mathit{Opx} + 0.06\,\mathit{Grt} + 1.00\,\mathit{melt} = 0.79\,\mathit{Cpx} + 0.44\,\mathit{Mca} + 0.38\,\mathrm{Qtz/Coe} \tag{12}$$

$$\mathit{Stage\ III}:\ 0.03\,\mathit{Opx} + 0.75\,\mathit{Cpx} + 1.00\,\mathit{melt} = 0.81\,\mathit{Am} + 0.47\,\mathit{Mca} + 0.50\,\mathrm{Qtz/Coe} \tag{13}$$

Here, we simulated further rock-melt reaction above the slab where a rhyolitic melt from the product of Stage I at 950°C infiltrates into the pyroxenite from experiment # G308 (Mallik *et al.*, 2015) at 3 GPa and 1050°C and 75–25 ratio. This reaction would represent Stage II above the slab. Unlike the Stage II reaction at 800°C and 75–25 ratio (Eq. 9), the pyroxenes do not participate in the melting reaction (consumed nor produced) but only mica and amphibole are consumed to produce garnet and melt.

$$\mathit{Stage\ II}: 3.00\,\mathit{Mca} + 5.50\,\mathit{Am} = 7.50\,\mathit{Grt} + 1.00\,\mathit{melt}. \tag{14}$$

DISCUSSION

The conditioning factors on silica activity in the melt ($a^{M}_{SiO_2}$) and the suppression or precipitation of olivine in mixed experiments (porous flow system)

An intriguing observation is that we produce exclusively olivine-free lithologies (mica-bearing pyroxenites ± amphibole± coesite±

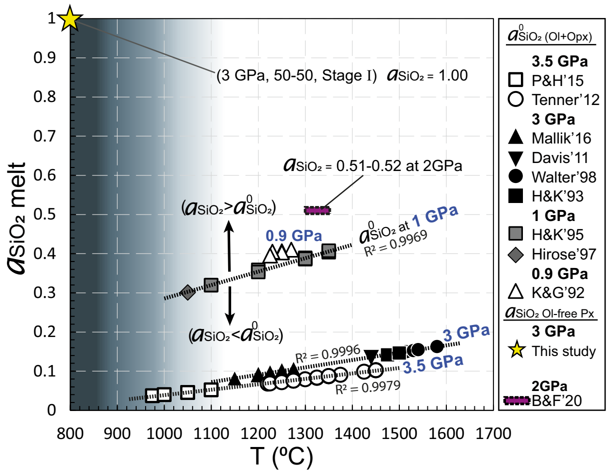

Fig. 4. $a^M_{SiO_2}$ vs. T compiled from published and new (this study) experimental data. The curves labeled 1 GPa, 3 GPa and 3.5 GPa are regression lines of the $a^0_{SiO_2}$, where Olivine and orthopyroxene (Ol + Opx) coexist with the melt at these *P*. At each curve, Ol precipitates at the expense of Opx below the curve ($a^M_{SiO_2} < a^0_{SiO_2}$) and vice-versa ($a^M_{SiO_2} > a^0_{SiO_2}$) above the curve, as indicated with the black arrows. The H_2O content in the literature is variable from volatile-free to up to 6 wt%; it is integrated in the $a^0_{SiO_2}$ term. The $a^0_{SiO_2}$ at 3 GPa is calculated from Davis *et al.* (2011), Hirose & Kushiro (1993), Mallik *et al.* (2016) and Walter (1998). The 3.5 GPa curve is calculated from Pirard & Hermann (2015) and Tenner *et al.* (2012). The data at 1 and 0.9 GPa are taken from Hirose & Kawamoto (1995) and Kinzler & Grove (1992), respectively. The lilac area delimited with black dashed line is the $a^0_{SiO_2}$ for pyroxenite-derived melts given by Borghini & Fumagalli (2020) at 2 GPa. The star symbols show $a^0_{SiO_2}$=1 for the melts formed at 800°C and 50–50 rock-melt ratio (quartz-coesite-saturated melt). The gradient area from white to dark gray color (right to left) illustrate the decreasing temperature from hotter mantle (>1300°C) toward the slab-mantle interface (800–950°C).

garnet/spinel) while other studies with similar rock-melt ratios, *P* and bulk H_2O contents have olivine in the residual assemblage (Mallik *et al.*, 2015; Pirard & Hermann, 2015; Mallik *et al.*, 2016; Zhang *et al.*, 2020b). We therefore examine the conditioning factors that affect the stability of residual olivine as follows. The precipitation or suppression of olivine has been related to the silica activity of the infiltrating melt ($a^M_{SiO_2}$) reacting with the lherzolite-mantle (Lambart *et al.*, 2009; Lambart *et al.*, 2012) such that if $a^M_{SiO_2}$ is lower than the silica activity of a melt saturated in olivine and orthopyroxene ($a^0_{SiO_2}$ at given *P* and *T*), it causes precipitation of olivine and suppression of orthopyroxene. But, if $a^M_{SiO_2}$ is higher than $a^0_{SiO_2}$ then olivine is suppressed and orthopyroxene precipitates. Moreover, low *P* (<2 GPa) and significant amount of H_2O in the system seem to favor the precipitation of olivine (Mallik *et al.*, 2015 and 2016). However, it is not clear how the interplay of *T*, *P*, peridotite composition, rock-melt ratio, and H_2O content controls the silica activity (a_{SiO_2}), and thus, the fate of olivine in the system. Although it is widely accepted that the silica activity in all partial melts in equilibrium with olivine and orthopyroxene ($a^0_{SiO_2}$) are fixed (buffered) and near constant (Dasgupta *et al.*, 2007; Lambart *et al.*, 2012; Mallik *et al.*, 2015, 2016), here we show that it does varies with *P* and *T* (Fig. 4). The $a^0_{SiO_2}$ of the melts that are olivine and orthopyroxene-saturated (e.g. lherzolite or harzburgite assemblage) is calculated from the following reaction:

$$\text{Ol (olivine)} + \text{SiO}_2\ \text{(melt)} \leftrightarrow \text{Opx (orthopyroxene)} \qquad (15)$$

The details about silica activity calculation for the reacted melts from literature can be found in Supplementary S.5.

Figure 4 shows that $a^0_{SiO_2}$ has a positive correlation with *T* and decreases with increasing *P*. For example, in the closely related 3–3.5 GPa curves, the $a^0_{SiO_2}$ increases from ∼0.03 to ∼0.17 when increasing from 975°C to ∼1650°C. This means that the stability field of olivine increases in area with increasing *T*. However, if *P* decreases to 1 GPa, the curve shifts higher and $a^0_{SiO_2}$ increases from ∼0.3 to ∼0.4 when *T* increases from 1100°C to 1350°C. Thus, the olivine stability field also expands by decreasing *P* which is corroborated by earlier experimental studies (Edgar, 1987; and references therein). An interesting observation is that H_2O contents of the melt, by themselves, do not affect $a^0_{SiO_2}$ along the olivine and orthopyroxene equilibrium since the melt compositions on each of the $a^0_{SiO_2}$ curves span from a range of volatile-free to hydrous compositions (Fig. 4). Rather hydrous partial melts in equilibrium with olivine and orthopyroxene form at lower *T*'s than volatile-free partial melts, hence, the dependence of $a^0_{SiO_2}$ on *T* captures the presence or absence of H_2O in the system.

On the other hand, quartz/coesite-saturated melts at 800°C and 3 GPa (e.g. MELT 1, 2 and 3 at 50–50; and MELT 2 and 3 at 75–25) must have a_{SiO_2}=1, as indicated in Fig. 4. If quartz/coesite are not present (e.g. MELT 1 at 75–25) we predict that the a_{SiO_2} is higher than $a^0_{SiO_2}$, and such melts are highly reactive with the peridotite mantle.

The effect of H_2O on the olivine stability has been investigated by Mallik *et al.* (2015 and 2016) at hotter conditions (1050–1350°C) in the sub-arc mantle wedge (2–3 GPa). Both studies used the same peridotite composition (KLB-1), and rock-melt ratio (75–25) as in our study, but with 1.8 wt% (Mallik *et al.*, 2015) to 6 wt% bulk H_2O content in the system (Mallik *et al.*, 2016). The run products in Mallik *et al.* (2015) at mantle-wedge core conditions (3 GPa and 1050–1350°C) are olivine-free, except for one experiment at 1100°C, where olivine appears as a trace phase. However, olivine is present in the residual assemblage when increasing the H_2O content in the system up to 6 wt% (Mallik *et al.*, 2016) which is similar to this study (5–7.5 wt% H_2O). However, unlike Mallik *et al.* (2016), olivine is not present in any rock-melt reaction product from this study. The only difference between the two studies is temperature. Mallik *et al.* (2016) investigated the rock-melt reactions at hotter conditions above the slab, and we investigated the same reactions but at slab-mantle interface conditions (800–950°C). Thus, it appears that stability of olivine due to melt-rock reactions in sub-arc conditions is favored at higher temperatures (near the core of the mantle wedge) rather than at the slab-mantle interface. The presence or absence of olivine in the residual assemblage determines the chemistry of the product melt in terms of $a^M_{SiO_2}$ (melt infiltration). For example, all else being similar, rock-melt reactions at the hotter core of the mantle wedge would produce magmas in equilibrium with olivine and orthopyroxene, thus their $a^M_{SiO_2} = a^0_{SiO_2}$. On the other hand, magmas formed near the slab-mantle interface (low *T*) would have their $a^M_{SiO_2} > a^0_{SiO_2}$ given only orthopyroxene is present in the residue. This condition produces more siliceous magmas than those formed in the hotter core, assuming $\gamma^M_{SiO_2}$ (activity coefficient of SiO_2 in the magma) are similar for the magmas at the slab-mantle interface and the hotter core of the mantle wedge. As evidence, experimental partial melts produced at the slab-mantle interface (800–1000°C), including those from this study, are highly silicic (>72–80 wt% SiO_2 on a volatile-free basis, Fig. 5) compared to partial melts produced at hotter mantle conditions (<72 wt% SiO_2).

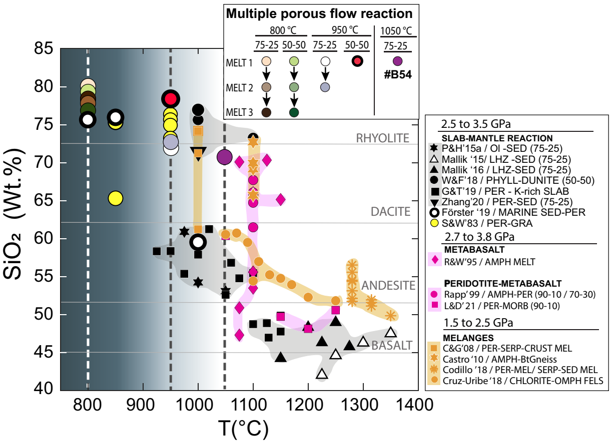

Fig. 5. SiO_2 of experimental melts vs. *T*. Compositional variations were produced over a range of *T* and *P*. All major elements in this figure are normalized to volatile-free and the rock-melt ratios are given in parenthesis in the legend. The lower *T* (800–950°C) melts show increase in SiO_2 compared with the melts produced at the core mantle. The gray, pink, and orange shaded areas delimit the chemistry domain of slab-mantle reaction partial melts, metabasalt partial melts and mélange partial melts, respectively. The hydrous partial melting at 2.5 and 3.5 GPa were taken from Pirard & Hermann (2015), Mallik *et al.* (2015), Mallik *et al.* (2016), Wang & Foley (2018), Grove & Till (2019), Zhang et al. (2020b), Förster *et al.* (2019)) and Sekine & Wyllie (1983). The metabasalt and peridotite-metabasalt partial melts at 2.7–3.8 GPa are from Rapp & Watson (1995), Rapp *et al.* (1999) and Lara & Dasgupta (2020). The mélange partial melts are from Castro & Gerya (2008), Castro *et al.* (2010), Codillo *et al.* (2018) and Cruz-Uribe *et al.* (2018). PER, peridotite; SED, sediment; SERP, serpentine; LHZ, lherzolite; GRA, granite; MEL, mélange; AMPH, amphibolite; OMPH, omphacite; PHYLL, phyllite; RHYO, rhyolite; PX, pyroxenite.

The composition of the mantle wedge peridotite is also an important factor. For example, Pirard & Hermann (2015) and Zhang *et al.* (2020b) performed porous flow experiments at similar *P*, *T*, and rock-melt ratios (75–25) as the experiments from this study and produced olivine. The only difference from our study is the chosen peridotite composition. Pirard & Hermann (2015) and Zhang *et al.* (2020b) used dunite (100% Ol) and harzburgite (82% Ol and 18% Opx), respectively, which are both richer in MgO (45.5–50 wt%), FeO (~9 wt%) and Mg# 90–92 than fertile peridotite. On the other hand, the KLB-1 lherzolite (61% Ol, 13.6% Opx, 12.5% Cpx, 11.9% Grt, and 1% Spl) used in this study is lower in MgO (39.5 wt%) and FeO (~8 wt%) relatively high Mg# 89 and high silica (~45 wt% SiO_2) as compared to dunite. As a result, the experimental melt compositions in Pirard & Hermann (2015) and Zhang *et al.* (2020b) are lower in silica (~53–72 wt% SiO_2) compared to our melts (~72–80 wt% SiO_2) and are consistent with a lower overall Si-activity in the mixed product, and thus, olivine is still present in their system.

The rock-melt ratio of the reaction is another factor that controls the transformation of a dunite/harzburgite lithology into an olivine-free lithology. For example, Wang & Foley (2018) performed porous flow experiments at similar *P*–*T* conditions as Pirard & Hermann (2015) and Zhang *et al.* (2020b) and used a natural clinopyroxene-bearing dunite (>95% Ol + 2% Spl + <1% Cpx) as a representative of a depleted peridotite and a natural quartz phyllite as a representative of continent-derived sediments. All these factors were similar to Pirard & Hermann (2015) and Zhang *et al.* (2020b). The only difference is that instead of 75–25 rock-melt ratio, Wang & Foley (2018) investigated 50–50 rock-melt ratio, simulating a larger influx of felsic partial melts into the system. The experiments from Wang & Foley (2018) produced orthopyroxene ± garnet ± coesite ± clinopyroxene at 3 GPa and 1000°C without any trace of olivine, which is consistent with the hypothesis that a low rock-melt ratio enhances a_{SiO_2} and thus suppresses olivine. Here, we corroborate the assumptions and predictions from previous studies that silica-excess systems (low rock-melt ratios) potentially form olivine-free pyroxenites (Rapp *et al.*, 1999; Straub *et al.*, 2011).

Pyroxenites as melt 'enabler' rather than a melt barrier

Partial melts from the slab with $a^M_{SiO_2} > a^0_{SiO_2}$ andrich in alkalis that infiltrate the basis of the mantle wedge via mechanical fracturing or hydrofracturing (Davies, 1999) are highly reactive with the overlying mantle and can form mica-rich pyroxenites (Lambart *et al.*, 2012, 2016; Borghini & Fumagalli, 2020). The focused reactive flow of hydrous slab melts through the mantle (e.g. fractures/veins) produce a distinct olivine-free rim composed of orthopyroxene ± garnet or clinopyroxene ± amphibole at the interface between the infiltrating melt and the subsolidus peridotitic wall-rock (Pirard & Hermann, 2015; Wang & Foley, 2018; Zhang *et al.*, 2020b; Förster *et al.*, 2019; Mallik & Dasgupta, 2012; Yaxley & Green, 1998). It can also potentially saturate quartz/coesite (Sekine & Wyllie, 1983). These studies confirm that the interaction between silicic slab components and the peridotite is highly reactive and may form rims that act as a barrier which prevents later melts from infiltrating further into the peridotite mantle due to the reduction of rock porosity (e.g. Lambart *et al.*, 2012). However, the implication that the pyroxenite formed due to rock-melt reaction would act as a barrier to later infiltrating melts stems from previous studies that explored one stage of rock-melt reaction (Stage I). Here, we envision a peridotite parcel (e.g. lherzolite) being repeatedly modified by hydrous-silicic slab partial melts (25–50 wt% melt) represented as stages I through III.

In this study, we observe that olivine is completely erased from the residue right from the first rock-melt reaction. But most importantly, after the second and third stages of slab-melt addition, the melt fraction and the rhyolitic composition of the melts reach constant melt fraction and SiO_2 values (~18–27 wt% and ~ 72–80 wt%, respectively) and the alkali content increases gradually (~1.6–8.2 wt%) to approach the JR-1 slab composition (Fig. 6, a, b and c) due to the continuous supply of alkalis from the slab-melt. At low *T* (800°C) and low rock-melt ratios (50–50) the melt fraction is lower (11–18 wt%) because quartz/coesite precipitates, but it does not change the composition of the reactant melts. Thus, rather than the pyroxenitic reaction rims being a 'barrier' to further infiltrating melts, they can act as an 'enabler' for incoming melts as they have the potential to act as pathways that allow 'continued passage' without consuming much of their mass or changing their composition during infiltration (Fig. 7).

To corroborate this observation that pyroxenite bodies may act as melt 'enablers' in the sub-arc mantle, we simulate another rock-melt reaction (75–25) where a hydrous-rhyolitic melt from Stage I (#B1110, melt 1) infiltrates and reacts with the pyroxenitic solid residue (#G308 from Mallik *et al.*, 2015) at 3 GPa and 1050°C (Fig. 7, denoted as area number 2). As expected, the reactant melt composition resembles the felsic infiltrating melt, and the melt fraction post-rock-melt reaction remains nearly unchanged (~23 wt% pre-rock-melt reaction to ~27 wt% after rock-melt reaction). These observations indicate that the solids would approach a melt-buffered state and that the slab-melts have higher chances

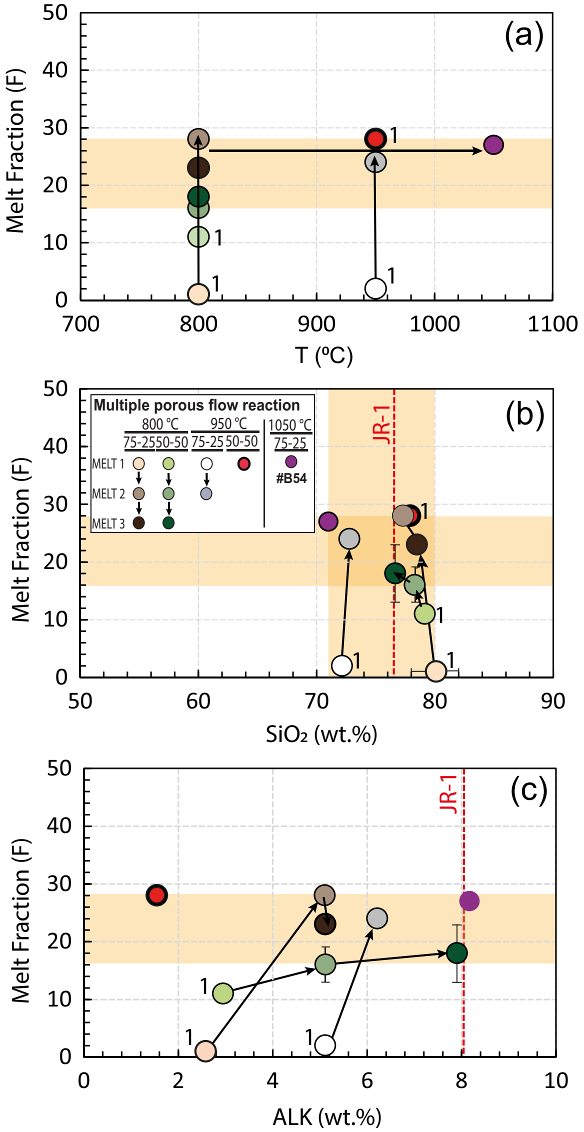

Fig. 6. Melt fraction (F) in wt% vs. T (°C), SiO_2, and alkalis (ALK: $K_2O + N_2O$ wt%). The number 1 near the symbols indicates the first reacted melts (MELT 1). The melt fraction (16–27%) and rhyolitic character (72–80 wt% SiO_2) of the melts remains almost constant after stage II through III as indicated with the horizontal and vertical orange shaded area. The alkali content of the initial reacted melt (MELT 1) is depleted due to the presence of K-bearing phases but resembles the original slab-partial melt (JR-1) due to the continuous alkali supply from the slab partial-melt (MELT 2 and 3). The error bars are smaller than the symbol sizes for certain data points.

to travel through those pyroxenite structures while avoiding compositional changes as well as further reactions with the mantle peridotite.

Effect of multiple stages of rock-melt reactions on the trace elements, H_2O/K_2O and H_2O/Ce ratios of slab-melts

While we established that slab melts preserve their first-order major element signature and mass during their passage through pyroxenites, do these slab melts also preserve their slab-derived trace element signatures along with their K_2O/H_2O and H_2O/Ce ratios during their transit? This is important to consider for reasons explained as follows. Plank & Langmuir (1993) noted

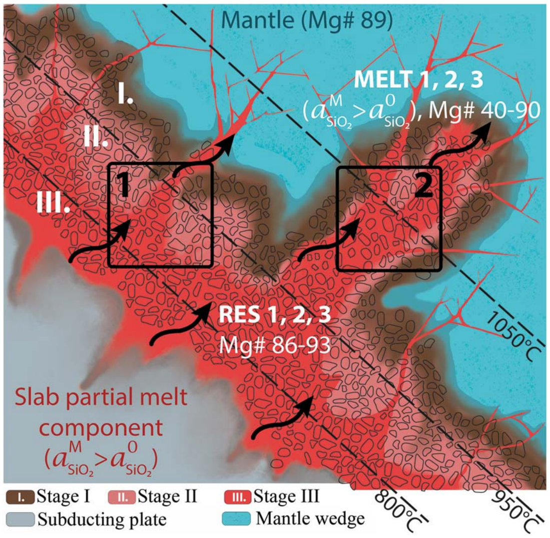

Fig. 7. Representation of a multiple stage process of rock-melt reaction (stages I–III) at intermediate to hot subduction zones (not to scale). The black quadrangle denoted '1' represents the near-slab top rock-melt reaction at 3 GPa (~90 km) and 800–950°C, initiated by the infiltration of the slab partial melt component (high$a^M_{SiO_2}$) and reacting with the mantle (a. stage I). This reaction forms a residue of mica-rich pyroxenite ± Am (RES 1) and a reacted melt (MELT 1) that leaves the system. A second influx from the slab transforms RES 1 into a Mca-pyroxenite ± Qrtz/Coe (RES 2) and produces a reacted melt (MELT 2). A third influx produces more Mca-rich pyroxenite ±Am ± Qrtz/coesite (decrease of pyroxenes wt%) and a reacted (MELT 3). The reacted melts (melts 1, 2 and 3) are compositionally alike to the slab partial melt component (JR-1) whereas the solid residues (RES 1, 2 and 3) evolve to low-dense mineralogy (rich in alkalis) but maintains a constant high Mg# (0.86–0.9) alike to the initial lherzolite (0.89). The black quadrangle denoted '2' represents the rock-melt reaction above the slab (3 GPa and 1050°C; from experiment #B54). The reactant melt (MELT 1) originated near the slab infiltrates toward hotter conditions (1050°C) and reacts with the above pyroxenitic lithology (residue from Mallik *et al.*, 2015). The above mantle may have structural weakness (dykes/veins) due to shear and normal forces where the melts can infiltrate further (channeled flow reaction).

positive correlations between sediment inputs and enrichment in arc volcanics for Ba, Sr, K, Rb, Cs, La, Th, and U across eight trenches around the globe, which are indicative of subducted sediment signatures being transferred to arc volcanics. Primitive trondhjemites from the Trans-Mexican Volcanic Belt show a strong slab signature (Gómez-Tuena *et al.*, 2008), indicating the role of the slab in its formation. The correlations between sediment inputs and trace elements in arc lavas as well as the slab signature in the trondhjemites would hold true if the slab trace element signature is not decoupled from that in the arc volcanics by some process during melt formation and ascent. Thus, it is important to assess whether trace element signatures of slab-derived melts are modified during their reactive transit through the sub-arc mantle. K_2O/H_2O and H_2O/Ce ratios have been used as slab thermometers (Hermann & Spandler, 2008; Plank *et al.*, 2009), whereby the estimated slab temperatures derived from these ratios in arc lavas appear to be in good agreement with predictions from thermal models (Cooper *et al.*, 2012). This indicates that the slab-melt should preserve these ratios during the reactive ascent through the sub-arc mantle to the crust. Based on this, Pirard & Hermann (2015) concluded that the porous flow of slab-melt and subsequent reaction with the sub-arc mantle near the slab-mantle interface resulted in the formation of phlogopite and amphibole which lowered the K_2O/H_2O ratio of the slab-melt and raised the H_2O/Ce ratio away

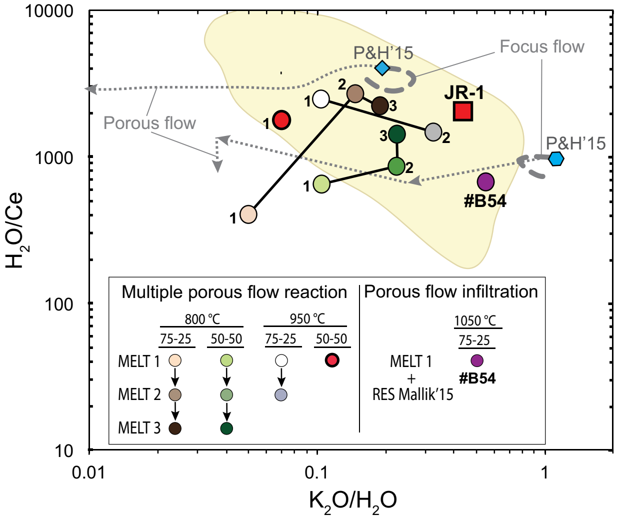

Fig. 8. H_2O/Ce vs K_2O/H_2O. Modified from Mallik *et al.* (2016) and Pirard & Hermann (2015). Thick-dashed line denotes the focus flow path, whereas the thin-dashed line is the path for porous flow reaction (only one stage) and the arrows indicates the direction toward lower *T*. The yellow-shaded is the natural arc lavas domain. Multiple porous flow resembles the slab composition (JR-1).

from the field of natural arc lavas (Fig. 8). On the other hand, the reactive channelized flow of slab-melts results in the formation of olivine and orthopyroxene which does not affect the ratios in slab-melts. Mallik *et al.* (2016) also noted that the reaction of slab-melts with the sub-arc mantle near the hotter core of the mantle wedge did not alter these ratios either because the principal mineral phases to form from the rock-melt reaction were olivine and orthopyroxene. Here we test the fate of trace elements and the K_2O/H_2O and H_2O/Ce ratios of slab-melts as they undergo multiple episodes of rock-melt reaction with the sub-arc mantle close to the slab-mantle boundary (800–950°C at 3 GPa) as well as away (1050°C at 3 GPa). The H_2O/K_2O and H_2O/Ce ratios of the melt compositions are reported in the Supplementary Information (excel).

Pirard & Hermann (2015) stated that porous flow of slab-melt through the sub-arc mantle near the slab-mantle interface results in the crystallization of phlogopite and amphibole. This would drive K_2O/H_2O and H_2O/Ce of the melt away from the field of natural arc lavas. Consequently, Pirard & Hermann (2015) argue that porous flow is not the mode of slab-melt transfer in the sub-arc mantle. In this study, we observe that the melt compositions from Stage I (equivalent to the porous flow experiments by Pirard & Hermann (2015), except they chose a dunite as representative of the sub-arc mantle) deviate in K_2O/H_2O and H_2O/Ce ratios from the initial slab-melt due to the crystallization of amphibole and phlogopite, and in most cases lie outside the field of natural arc lavas. Hence, Stage I rock-melt reaction would (a) alter the slab-top signature in the melt post rock-melt reaction thus hindering the transfer of slab signatures to the arc lavas and, (b) drive the H_2O/K_2O and H_2O/Ce ratios outside the field of natural arc lavas. Thus, if these ratios were used to determine the slab-top temperature, they would produce erroneous results. However, as subsequent stages of melt-rock reaction take place from Stages II through III, the melting out of amphibole and mica drives the melt compositions back toward the initial slab-melt in H_2O/K_2O and H_2O/Ce ratios. One single rock-melt reaction (stage I) can alter the slab trace-pattern as demonstrated by Pirard & Hermann (2015) but additional episodes of porous-flow rock-melt reactions are important for preserving slab signatures as well as the viability and reliability of slab thermometers.

Mass balance dictates that at given slab-mantle mixing proportions, JR-1 should dominate the trace element signature of the reactant melts. Figure 9 shows that the rhyolitic reactant melts potentially adopt the slab signature (e.g. JR-1) after successive influx of fresh slab partial melt (stages I through III). Due to a higher proportion of slab-melt in the system, the reactant melts formed at 50–50 rock-melt ratio resemble the geochemical signature of JR-1 more strongly than the reactant melts formed at 75–25 rock-melt ratio across stages I to III. However, at high rock-melt (75–25) ratios the first reactant melt (MELT 1) at 800, 950 and 1050°C show LILE and HREE depletion to some extent, and HFSE and LREE enrichment due to the presence of garnet and hydrous minerals (mica and amphibole). However, the subsequent reactant melts (MELT 2 and 3) recover the slab-signature by the incoming fresh slab-melt. Therefore, trace element composition of the reactant melts trace-composition in both rock-melt scenarios (50–50 and 75–25) end up resembling the slab-signature. The presence of quartz/coesite and pyroxenes does not affect the slab signature. The batch melting modeling is explained in Supplementary S.6.

However, our proxy to slab partial melts (JR-1) does not have an initial garnet signature (Ando *et al.*, 1989). Schmidt & Jagoutz (2017) observed a depletion in HREEs in primitive arc melts compared to N-MORB globally and attributed this to a depleted signature in the sub-arc mantle rather than a garnet signature. We note that a slab-melt would have potential HREE depletion due to residual garnet in the slab (Hermann & Spandler, 2008; Rapp & Watson, 1995; Straub *et al.*, 2014; Gómez-Tuena *et al.*, 2008), hence primary arc magmas with contributions from slab melts would have a garnet signature to begin with. Multiple episodes of rock-melt reaction near the slab-mantle interface (800–950°C at 3 GPa) by flushing slab-melt to the peridotite and consequent pyroxenitic mantle (1050°C at 3 GPa) would reinforce the slab garnet signature in the resultant melt compositions (Fig. 10). Therefore such repeated rock-melt reactions occurring at depths ~90 km (3 GPa) help in preserving slab signatures that may be passed on to primitive arc melts. In addition, Turner & Langmuir (2022) noted a positive correlation between HREE depletion (using Dy/Yb as a proxy) in high Mg# arc lavas and crustal thickness in the overlying lithosphere and attributed it to residual garnet in the mantle wedge under continental arcs (thicker crust) rather than island arcs (thinner crust). An alternative explanation of the degree of HREE depletion with crustal thickness maybe as follows: arcs with thicker crust and shallower slab dips have an overall shorter 'pathway' from slab to the Moho in the overlying lithosphere (e.g. the Cascades) compared to island arcs with thinner arcs and steep dipping slabs (e.g. Tonga). Our trace element batch melting model (See Supplementary S.7) demonstrates that the first reactant melt (MELT 1) that has garnet signature will gradually dilute when interacting with a fertile (Xu, 2000) or even with a depleted mantle (Straub *et al.*, 2014). This observation would imply that a longer 'pathway' through the mantle would result in greater reduction in garnet signature (such as beneath Tonga) compared to a shorter pathway (such as beneath Cascadia). Future studies investigating the correlation between HREE depletion and 'pathway' length in the sub-arc mantle across arcs would validate this hypothesis. The batch melting modeling and the garnet-slab signature modeling results can be found in Supplementary Information, excel).

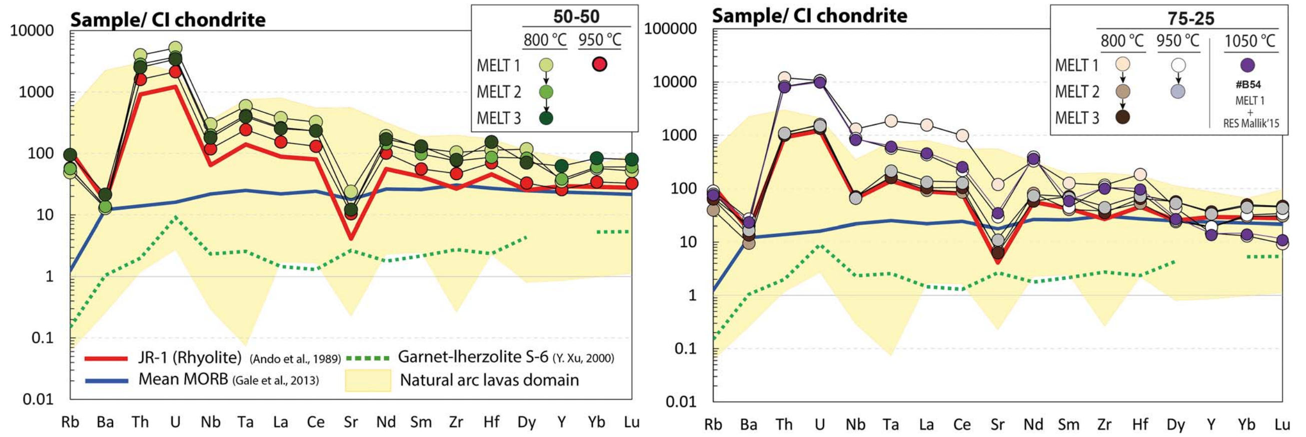

Fig. 9. CI-chondrite normalized (McDonough & Sun, 1995) incompatible trace element patterns for the reactant melts (MELT 1, 2, 3) at the slab-mantle interface. The trace element patterns are predicted using the batch melting equation (see Supplementary S7). The figure on the left is the trace element-pattern through successive high slab-influx (50–50) and the figure on the right corresponds to the successive low slab influx (75–25). Note our proxy for the slab influx that does not have an initial garnet signature (JR-1).

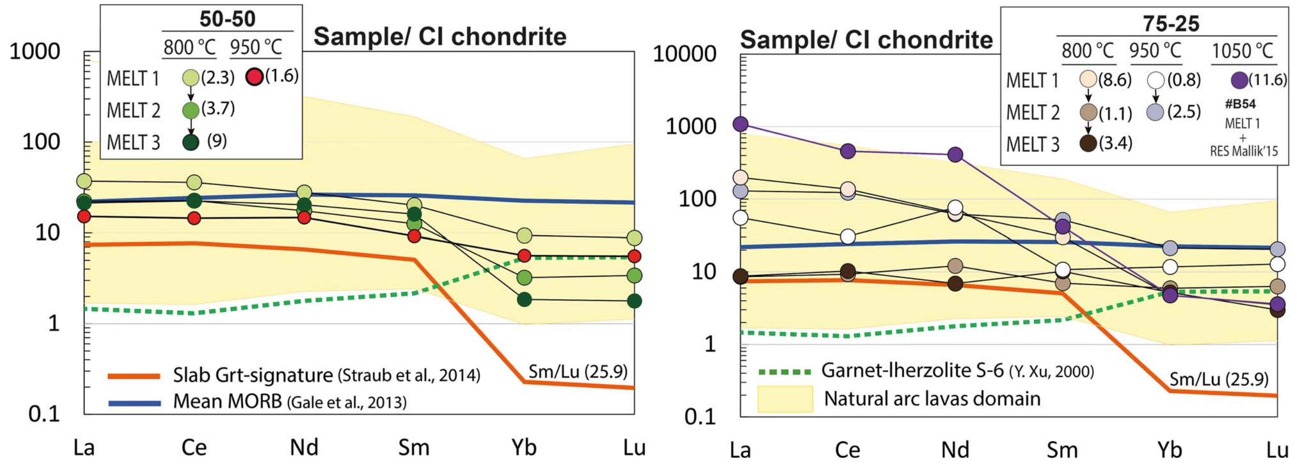

Fig. 10. Predicted trace element patterns for the reacted melts (MELT 1, 2, 3) using an initial slab partial melt with Grt signature (strong HREE depletion). CI-chondrite normalized (McDonough & Sun, 1995). Check Supplementary Information for further information on the batch melting calculation. The number in parentheses indicates the Sm/Lu ratios. The figure on the left is the trace element-pattern through successive high slab influx (50–50) and the figure on the right corresponds to the successive low slab influx (75–25). Note that in this scenario, our proxy for the slab influx does have an initial garnet signature.

The formation of low dense reacted melts and pyroxenites at the slab-mantle interface

The successive additions of silica, alkalis, H_2O and alumina from the slab promote the formation of low-density volatile-bearing phases like mica (ρ ~2.7 g/cm^3), amphibole (ρ ~3.1 g/cm^3) and the eventual precipitation of quartz/coesite (ρ ~2.9 g/cm^3) (Fig. 11 and Table 3). Because they are less dense than the average mantle wedge peridotite (~3350 kg/m^3), they may potentially form instabilities resulting in diapiric structures at the base of the wedge (Hall & Kincaid, 2001; Marschall & Schumacher, 2012; Nielsen & Marschall, 2017; Cruz-Uribe *et al.*, 2018). To estimate the density contrast between the hydrous pyroxenites formed in this study via rock-melt reaction to the peridotite mantle wedge, we calculated the bulk density of the peridotite mantle at 3 GPa and 800–950°C from MELTS (Gualda & Ghiorso, 2015) by using the modal mineralogy of KLB-1 (61% olivine, 13.6% orthopyroxene, 12.5% clinopyroxene, 11.9% garnet, and 1% spinel), which is similar to that of the primitive mantle (57% olivine, 16% orthopyroxene, 14% clinopyroxene, 13% garnet) reported in Mcdonough & Rudnick (1998). The bulk residue density in each experiment was calculated using the ´modified Tait EOS´ (Holland & Powell, 2011) and the phase proportions obtained from this study (See Supplementary S.8).

The estimated bulk residue at 3 GPa and 950°C at both rock-melt ratios (75–25 and 50–50) has an average density of ~3270 ± 19 kg/m^3 (Table 3) which is not significantly less dense than mantle wedge peridotite. However, at 800°C the densities of the residue and melt are controlled by the rock-melt ratio investigated. For example, at 800°C and 75–25 (stage I through III) the residue density varies between 3385 ± 7 (Grt-present) to 3215 ± 26 kg/m^3, whereas with a smaller rock-melt ratio (50–50), the residue density decreases from 3187 ± 23 to 2943 ± 11 kg/m^3 (stages I through III). Therefore, the bulk residue shows an overall progressive decrease in density (from 3385 to 2943 kg/m^3) relative to the average mantle wedge density (~3350 kg/m^3) and slab eclogite (~3400 kg/m^3) (Zhang *et al.*, 2020a). The densities of the melts produced at 3 GPa and 800–950°C were calculated using the program *DensityX* from Iacovino & Till (2019). The density of our melts is calculated to be ~3200 ± 100 kg/m^3 if we consider water-free melts, and as low as ~2600 ± 200 kg/m^3 if hydrous

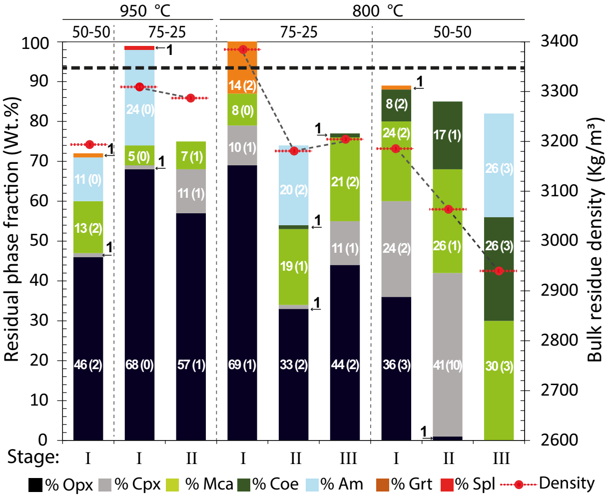

Fig. 11. Residual phase fraction and the calculated bulk solid residue density for each experiment. The presence of low-density minerals (mica, amphibole and quartz/coesite) lowers the bulk residue density significantly. The small black arrow with the number 1 indicates that the phase was not detected by mass balance but is present as trace residue. The number in parentheses indicates the SD ± 1σ value. The residue and the melt (blank space) sum 100 wt%. The horizontal, black dashed line shows the average lherzolite density (kg/m^3).

melts are considered. Therefore, both residue and melts display a plausible density contrast of ~150–400 kg/m^3 with the overlying mantle wedge. Numerical modeling shows that in both hot or cold subduction zones, low density material can detach from the slab at $T < 1050°C$ and rise into the hotter mantle (Hall & Kincaid, 2001; Gerya & Yuen, 2003; Miller & Behn, 2012). Although there is a noticeable density contrast between the reactant residues and melt with the mantle, the growth rate of the diapir is ultimately governed by the viscosity contrast and the thickness of the metasomatized layer (Behn *et al.*, 2011; Hack & Thompson, 2011; Miller & Behn, 2012). If buoyancy is favorable then, these type of metasomatic residues (51–68 wt% SiO_2, Mg# 0.86–0.9) and felsic-alkalic melts (>70 wt% SiO_2, Mg# 0.4–0.9) may ascend to the core of the mantle wedge where they would encounter further partial melting (Marschall & Schumacher, 2012).

Formation of high SiO_2 high mg# melt compositions in the sub-arc mantle

Entrapped rhyolitic melts are recently found as interstitial glasses in peridotite xenoliths (Dallai *et al.*, 2022). These melts are derived from the partial melting of continental crustal material (garnet-bearing metapelites) that interacted to some extent with the peridotite mantle — supporting the presence of rhyolitic melts in the sub-arc mantle.

Here, we propose that those rhyolitic melts can travel freely within 'enabler' pyroxenites, preserving the major and trace element signature from the slab-melt toward the hotter mantle wedge. However, the melts originated at the slab-mantle interface show high SiO_2 (74–82 wt%) and extremely low FeO (>2 wt%) and CaO (>2 wt%) compared to the erupted high-SiO_2 (56–70 wt%) and high-Mg# (50–70) global arc magmas (Fig. 12). The fresh rhyolitic partial melt (JR-1) is deficient in MgO, CaO, and FeO to begin with, and is transmitted to the reacted melts (MELT 1, 2, and 3). Therefore, elements like Mg, Ca, and Fe need to be supplied from another source either through mixing or assimilation with partial melts derived from altered oceanic crust in the slab (Rapp & Watson, 1995) or by mixing with peridotite somewhere in the hotter mantle wedge (Mallik *et al.*, 2015, 2016, 2021).

The experimental melts show some similarities with the intrusive high-silica Miocene-age trondhjemite found in Mexico (Gómez-Tuena *et al.*, 2008) that display a characteristic high SiO_2 (>70 wt%), low CaO (<3.8 wt%), FeO (<2.2 wt%) and MgO (<2.5 wt% and >4 wt% for trondhjemites and melts, respectively)—although these trondhjemites are high in Na_2O (6–6.5 wt%) and low K_2O (<0.8 wt%) compared to our reacted melts (~0.5–3 wt% Na_2O and 1–5 wt% K_2O). The discovery of these trondhjemites with strong slab melt signatures, may indicate that primitive magmas originating at the slab-mantle interface can reach crustal levels without undergoing extensive fractionation or assimilation during ascent. Thus, primitive magmas formed at the base of the mantle wedge may find their way up to crustal levels and contribute to the modern-arc diversity. Further exploration of multiple rock-melt reactions into the hotter mantle is required to explore the fate of those slab-melts and corroborate our observations and hypothesis of slab-melt 'survival'.

CONCLUSIONS

Complex mantle fertilization by multiple slab-melt porous flows is a potential mechanism for slab-melt infiltration into the mantle wedge. Such reactive processes lead to the formation of olivine-free and mica-rich pyroxenites ±amphibole ± quartz/coesite (with Mg# similar to the mantle) and hydrous-rhyolitic melts (72–80 wt% SiO_2 and 40–90 Mg#). This work corroborates that abundant precipitation of orthopyroxene and olivine suppression occurs at the slab-mantle interface enhanced by low temperatures and high pressures. Besides, the evident melt-buffered state of those pyroxenites indicates that slab-melts can pass freely through such lithologies, preserving their major (alkalis, Mg, Fe, Ca) and trace elements' slab signature. Thus, the pyroxenites potentially act as melt 'enablers' that help the slab-melts to infiltrate almost 'unmodified' deep into the mantle wedge. Also, the notable density contrast between the reactant lithologies (mica-rich pyroxenites) and melts relative to the mantle wedge and eclogitic slab, may initiate instabilities that lead to the diapiric ascent of slab-material and expedite the ascending into the mantle. We suspect that the pathway length from the slab through the mantle controls the diverse increments of Mg, Fe, and Ca, as well as the degree of HREE dilution in the melts. The existence of high-Mg# Miocene-Mexican-trondhjemites with strong slab signature are evidence of the capacity of almost pristine slab melts to reach crustal levels without extensive fractionation or assimilation. These observations may imply that some arc magmas originate from a common primitive magma at or near the slab-mantle interface and had different extents of interaction with the mantle while ascending. This would also explain the observed wide chemistry in primitive arc lavas and their variable degrees of slab-garnet signature. Most importantly, we can associate those high-Mg# andesites as the most pristine or 'unmodified' of all arc magma spectrum. Further exploration of multiple rock-melt interactions at hotter mantle conditions is required to corroborate our findings and hypothesis.

FUNDING

AMR acknowledges the international research and training group Deep Earth Volatile Cycles, Deutsche Forschungsgemeinschaft grant [GRK 2156/1], the Graduate & Professional Student Council

Research and Project (ReaP) Grant, and the Spencer R. Titley scholarship. AM acknowledges Alexander von Humboldt postdoctoral fellowship and National Science Foundation grant [EAR 2138410]. SMS acknowledges support from National Science Foundation grant [EAR 19–21624].

DATA AVAILABILITY

The experimental run product details are included in the article. The global MORB data are from Gale *et al.* (2013) and the global arc is a compilation data from Straub, S.M. (2019 and 2017) and from the GeoROC Database (https://georoc.eu/).

ACKNOWLEDGEMENTS

We thank Rafael Njul, Heinz Fischer and Stefan Übelhack for sample and assembly preparation, Catherine McCammon and Sumith Abeykoon for assistance with piston cylinder experiments, Hans Keppler for FTIR analyses, Dorothea Wiesner for assistance with the SEM, Detlef Krauße and Sumith Abeykoon for assistance with the EMPA at BGI. We also thank Ken Domanik for EMPA assistance at LPL (Michael J. Drake lab) and Zachary Michels for SEM assistance at the Arizona LaserChron Center. We thank Zoe Zeszut for Raman assistance at LPL.

We thank Sarah Lambart, Jay Quade, and the members of *Mallik Petrology Group* for very helpful discussions about the project. Last but not least, we also want to thank Madeleine Humphreys for her constructive reviews and editorial handling, along with Stephen Turner, Tom Sisson, and an anonymous reviewer for their feedback and comments that helped to clarify and improve this manuscript.

References

Abers, G. A., van Keken, P. E. & Wilson, C. R. (2020). Deep decoupling in subduction zones: observations and temperature limits. *Geosphere* **16**, 1408–1424. https://doi.org/10.1130/GES02278.1.

Anderson, A. T. (1974). Evidence for a picritic, volatile-rich magma beneath Mt. Shasta, California. *Journal of Petrology* **15**, 243–267. https://doi.org/10.1093/petrology/15.2.243.

Ando, A., Kamioka, H., Terashima, S. & Itoh, S. (1989). 1988 values for GSJ "igneous rock reference rock series" samples. *Geochemical Journal* **23**, 143–148. https://doi.org/10.2343/geochemj.23.143.

Baker, M. B. & Stolper, E. M. (1994). Determining the composition of high-pressure mantle melts using diamonds aggregates. *Geochimica et Cosmochimica Acta* **58**, 2811–2827. https://doi.org/10.1016/0016-7037(94)90116-3.

Ballhaus, C., Berry, R. F. & Green, D. H. (1991). High pressure experimental calibration of the olivine-orthopyroxene-spinel oxygen geobarometer: implications for the oxidation state of the upper mantle. *Contributions to Mineralogy and Petrology* **107**, 27–40. https://doi.org/10.1007/BF00311183.

Barr, J. A. & Grove, T. L. (2010). AuPdFe ternary solution model and applications to understanding the fO_2 of hydrous, high?pressure experiments. *Contributions to Mineralogy and Petrology* **160**, 631–643. https://doi.org/10.1007/s00410?010?0497?z.

Behn, M. D., Kelemen, P. B., Hirth, G., Hacker, B. R. & Massonne, H. J. (2011). Diapirs as the source of the sediment signature in arc lavas. *Nature Geoscience* **4**, 641–646. https://doi.org/10.1038/ngeo1214.

Beier, C., Haase, K. M., Brandl, P. A. & Krumm, S. H. (2017). Primitive andesites from the Taupo Volcanic Zone formed by magma mixing. *Contributions to Mineralogy and Petrology* **172**, 1–14.

Bindeman, I. N., Ponomareva, V. V., Bailey, J. C. & Valley, J. W. (2004). Volcanic arc of Kamchatka: a province with high-δ18O magma sources and large-scale 18O/16O depletion of the upper crust. *Geochimica et Cosmochimica Acta* **68**, 841–865. https://doi.org/10.1016/j.gca.2003.07.009.

Borg, L. E., Clynne, M. A. & Bullen, T. D. (1997). The variable role of slab-derived fluids in the generation of a suite of primitive calc-alkaline lavas from the Southernmost Cascades, California. *Canadian Mineralogist* **35**, 425–452.

Borghini, G. & Fumagalli, P. (2020). Melting relations of anhydrous olivine-free pyroxenite Px1 at 2 GPa. *European Journal of Mineralogy* **32**, 251–264. https://doi.org/10.5194/ejm-32-251-2020.

Bryant, J. A., Yogodzinski, G. M. & Churikova, T. G. (2011). High-Mg# andesitic lavas of the Shisheisky Complex, Northern Kamchatka: implications for primitive calc-alkaline magmatism. *Contributions to Mineralogy and Petrology* **161**, 791–810. https://doi.org/10.1007/s00410-010-0565-4.

Bullen, T. D. & Clynne, M. A. (1990). Trace element and isotopic constraints on magmatic evolution at Lassen volcanic center. *Journal of Geophysical Research* **95**, 19671. https://doi.org/10.1029/JB095iB12p19671.

Cameron, E., Gamble, J., Price, R., Smith, I., McIntosh, W. & Gardner, M. (2010). The petrology, geochronology and geochemistry of Hauhungatahi volcano, S.W. Taupo Volcanic Zone. *Journal of Volcanology and Geothermal Research* **190**, 179–191. https://doi.org/10.1016/j.jvolgeores.2009.07.002.

Carmichael, I. S. E. (2002). The andesite aqueduct: perspectives on the evolution of intermediate magmatism in west-central (105-99°W) Mexico. *Contributions to Mineralogy and Petrology* **143**, 641–663. https://doi.org/10.1007/s00410-002-0370-9.

Carroll, M. R. & Wyllie, P. J. (1989). Experimental phase relations in the system tonalite-peridotite-H_2O at 15 kb; implications for assimilation and differentiation processes near the crust-mantle boundary. *Journal of Petrology* **30**, 1351–1382. https://doi.org/10.1093/petrology/30.6.1351.

Castro, A. & Gerya, T. V. (2008). Magmatic implications of mantle wedge plumes: experimental study. *Lithos* **103**, 138–148. https://doi.org/10.1016/j.lithos.2007.09.012.

Castro, A., Gerya, T. V., García-Casco, A., Fernández, C., Diaz-Alvarado, J., Moreno-Ventas, I. & Löw, I. (2010). Melting relations of MORB-sediment mélanges in underplated mantle wedge plumes. Implications for the origin of cordilleran-type batholiths. *Journal of Petrology* **51**, 1267–1295. https://doi.org/10.1093/petrology/egq019.

Codillo, E. A., Le Roux, V. & Marschall, H. R. (2018). Arc-like magmas generated by mélange-peridotite interaction in the mantle wedge. *Nature Communications* **9**, 2864. https://doi.org/10.1038/s41467-018-05313-2.

Cooper, L. B., Ruscitto, D. M., Plank, T., Wallace, P. J., Syracuse, E. M. & Manning, C. (2012). Global variations in H_2O/Ce: 1. Slab surface temperatures beneath volcanic arcs. *Geochemistry, Geophysics* **570**, *Geosystems* **13** Q03024. https://doi.org/10.1029/2011GC003902.

Cruz-Uribe, A. M., Marschall, H. R., Gaetani, G. A. & Le Roux, V. (2018). Generation of alkaline magmas in subduction zones by partial melting of mélange diapirs—an experimental study. *Geology* **46**, 343–346. https://doi.org/10.1130/G39956.1.

Dallai, L., Bianchini, G., Avanzinelli, R., Deloule, E., Natali, C., Gaeta, M., Cavallo, A. & Conticelli, S. (2022). Quartz-bearing rhyolitic melts in the Earth's mantle. *Nature Communications* **13**. https://doi.org/10.1038/s41467-022-35382-3.

Dasgupta, R., Hirschmann, M. M. & Smith, N. D. (2007). Partial melting experiments of peridotite + CO_2 at 3 GPa and genesis of alkalic ocean island basalts. *Journal of Petrology* **48**, 2093–2124. https://doi.org/10.1093/petrology/egm053.

Davies, H. J. (1999). The role of hydraulic fractures and intermediate-depth earthquakes in generating subduction-zone magmatism. *Nature* **398**, 142–145. https://doi.org/10.1038/18202.

Davis, F. A., Hirschmann, M. M. & Humayun, M. (2011). The composition of the incipient partial melt of garnet peridotite at 3GPa and the origin of OIB. *Earth and Planetary Science Letters* **308**, 380–390. https://doi.org/10.1016/j.epsl.2011.06.008.

Davis, F. A., Tangeman, J. A., Tenner, T. J. & Hirschmann, M. M. (2009). The composition of KLB-1 peridotite. *American Mineralogist* **94**, 176–180. https://doi.org/10.2138/am.2009.2984.

Díaz-Bravo, B. A., Gómez-Tuena, A., Ortega-Obregón, C. & Pérez-Arvizu, O. (2014). The origin of intraplate magmatism in the western trans-Mexican volcanic belt. *Geosphere* **10**, 340–373. https://doi.org/10.1130/GES00976.1.

Edgar, A. D. (1987). The genesis of alkaline magmas with emphasis on their source regions: inferences from experimental studies (review paper). *Geological Society - Special Publications* **30**, 29–52. https://doi.org/10.1144/GSL.SP.1987.030.01.04.

Elliott, T., Plank, T., Zindler, A., White, W. & Bourdon, B. (1997). Element transport from slab to volcanic front at the Mariana arc. *Journal of Geophysical Research: Solid Earth* **102**, 14991–15019. https://doi.org/10.1029/97JB00788.

Förster, M. W., Foley, S. F., Alard, O. & Buhre, S. (2019). Partitioning of nitrogen during melting and recycling in subduction zones and the evolution of atmospheric nitrogen. *Chemical Geology* **525**, 334–342. https://doi.org/10.1016/j.chemgeo.2019.07.042.

Förster, M. W., Prelević, D., Schmück, H. R., Buhre, S., Veter, M., Mertz-Kraus, R., Foley, S. F. & Jacob, D. E. (2017). Melting and dynamic metasomatism of mixed harzburgite + glimmerite mantle source: implications for the genesis of orogenic potassic magmas. *Chemical Geology* **455**, 182–191. https://doi.org/10.1016/j.chemgeo.2016.08.037.

Gale, A., Dalton, C. A., Langmuir, C. H., Su, Y. & Schilling, J. G. (2013). The mean composition of ocean ridge basalts. *G-cubed* **14**, 489–518. https://doi.org/10.1029/2012GC004334.

Gerya, T. V. & Yuen, D. A. (2003). Rayleigh-Taylor instabilities from hydration and melting propel "cold plumes" at subduction zones. *Earth and Planetary Science Letters* **212**, 47–62. https://doi.org/10.1016/S0012-821X(03)00265-6.

Goltz, A. E., Krawczynski, M. J., Gavrilenko, M., Gorbach, N. V. & Ruprecht, P. (2020). Evidence for superhydrous primitive arc magmas from mafic enclaves at Shiveluch volcano, Kamchatka. *Contributions to Mineralogy and Petrology* **175**(12), 1–26. https://doi.org/10.1007/s00410-020-01746-5.

Gómez-Tuena, A., Langmuir, C. H., Goldstein, S. L., Straub, S. M. & Ortega-Gutiérrez, F. (2007). Geochemical evidence for slab melting in the trans-Mexican volcanic belt. *Journal of Petrology* **48**, 537–562. https://doi.org/10.1093/petrology/egl071.

Gómez-Tuena, A., Mori, L., Rincón-Herrera, N. E., Ortega-Gutiérrez, F., Solé, J. & Iriondo, A. (2008). The origin of a primitive trondhjemite from the trans-Mexican Volcanic Belt and its implications for the construction of a modern continental arc. *Geology* **36**, 471–474. https://doi.org/10.1130/G24687A.1.

Gómez-Tuena, A., Mori, L. & Straub, S. M. (2018b). Geochemical and petrological insights into the tectonic origin of the Transmexican Volcanic Belt. *Earth-Science Reviews* **183**, 153–181. https://doi.org/10.1016/j.earscirev.2016.12.006.

Gómez-Tuena, A., Straub, S. M. & Zellmer, G. F. (2014). An introduction to orogenic andesites and crustal growth. *Geological Society Special Publication* **385**, 1–13. https://doi.org/10.1144/SP385.16.

Gómez-Tuena, A. *et al.* (2018a). Generation of alkaline magmas in subduction zones by partial melting of mélange diapirs—an experimental study. *Journal of Petrology* **46**, 343–346. https://doi.org/10.1130/G39956.1.

Green, T. H. & Ringwood, A. E. (1967). Crystallization of basalt and andesite under high pressure hydrous conditions. *Earth and Planetary Science Letters* **3**, 481–489. https://doi.org/10.1016/0012-821X(67)90083-0.

Grove, T., Parman, S., Bowring, S., Price, R. & Baker, M. (2002). The role of an H_2O-rich fluid component in the generation of primitive basaltic andesites and andesites from the Mt. Shasta region, N California. *Contributions to Mineralogy and Petrology* **142**, 375–396. https://doi.org/10.1007/s004100100299.

Grove, T. L. & Till, C. B. (2019). H_2O-rich mantle melting near the slab–wedge interface. *Contributions to Mineralogy and Petrology* **174**, 1–22.

Grove, T. L., Till, C. B. & Krawczynski, M. J. (2012). The role of H_2O in subduction zone magmatism. *Annual Review of Earth and Planetary Sciences* **40**, 413–439. https://doi.org/10.1146/annurev-earth-042711-105310.

Gualda, G. A. R. & Ghiorso, M. S. (2015). MELTS_Excel: a Microsoft Excel-based MELTS interface for research and teaching of magma properties and evolution. *Geochemistry, Geophysics, Geosystems* **16**, 315–324. https://doi.org/10.1002/2014GC005545.

Hack, A. C. & Thompson, A. B. (2011). Density and viscosity of hydrous magmas and related fluids and their role in subduction zone processes. *Journal of Petrology* **52**, 1333–1362. https://doi.org/10.1093/petrology/egq048.

Hall, P. S. & Kincaid, C. (2001). Diapiric flow at subduction zones: a recipe for rapid transport. *Science* **292**, 2472–2475. https://doi.org/10.1126/science.1060488.

Hauri, E. H. (1996). Major-element variability in the Hawaiian mantle plume. *Nature* **382**, 415–419. https://doi.org/10.1038/382415a0.

Hawkesworth, C. J., Gallagher, K., Hergt, J. M. & McDermott, F. (1993). Mantle and slab contributions in arc magmas. *Annual Review of Earth and Planetary Sciences* **21**, 175–204. https://doi.org/10.1146/annurev.ea.21.050193.001135.

Hermann, J. & Spandler, C. J. (2008). Sediment melts at sub-arc depths: an experimental study. *Journal of Petrology* **49**, 717–740. https://doi.org/10.1093/petrology/egm073.

Hirose, K. (1997). Melting experiments on lherzolite KLB-1 under hydrous conditions and generation of high-magnesian andesitic melts. *Geology* **25**, 42–44. https://doi.org/10.1130/0091-7613(1997)025<0042:MEOLKU>2.3.CO;2.

Hirose, K. & Kawamoto, T. (1995). Hydrous partial melting of lherzolite at 1 GPa: the effect of H_2O on the genesis of basaltic magmas. *Earth and Planetary Science Letters* **133**, 463–473. https://doi.org/10.1016/0012-821X(95)00096-U.

Hirose, K. & Kushiro, I. (1993). Partial melting of dry peridotites at high pressures: determination of compositions of melts segregated from peridotite using aggregates of diamond. *Earth and Planetary Science Letters* **114**, 477–489. https://doi.org/10.1016/0012-821X(93)90077-M.

Holland, T. J. B. & Powell, R. (2011). An improved and extended internally consistent thermodynamic dataset for phases of petrological interest, involving a new equation of state for solids. *Journal of Metamorphic Geology* **29**, 333–383. https://doi.org/10.1111/j.1525-1314.2010.00923.x.

Iacovino, K. & Till, C. B. (2019). DensityX: a program for calculating the densities of magmatic liquids up to 1,627 °C and 30 kbar. *Volcanica* **2**, 1–10. https://doi.org/10.30909/vol.02.01.0110.

Kägi, R., Müntener, O., Ulmer, P. & Ottolini, L. (2005). Piston-cylinder experiments on H_2O undersaturated Fe-bearing systems: an experimental setup approaching fO2 conditions of natural calc-alkaline magmas. *American Mineralogist* **90**, 708–717. https://doi.org/10.2138/am.2005.1663.

Kelemen, P. B. (1995). Genesis of high Mg# andesites and the continental crust. *Contributions to Mineralogy and Petrology* **120**, 1–19. https://doi.org/10.1007/BF00311004.

Kelemen, P. B., Hanghøj, K. & Greene, A. R. (2014). One view of the geochemistry of subduction-related magmatic arcs, with an emphasis on primitive andesite and lower crust. *Treatise on Geochemistry* **3**, 749–806. https://doi.org/10.1016/B978-0-08-095975-7.00323-5.

Kinzler, R. J. & Grove, T. L. (1992). Primary magmas of mid-ocean ridge basalts 2. Applications. *Journal of Geophysical Research* **97**, 6907–6926. https://doi.org/10.1029/91JB02841.

Kogiso, T., Hirschmann, M. M. & Pertermann, M. (2004). High-pressure partial melting of mafic lithologies in the mantle. *Journal of Petrology* **45**, 2407–2422. https://doi.org/10.1093/petrology/egh057.

Kushiro, I. (1972). Effect of water on the composition of magmas formed at high pressures. *Journal of Petrology* **13**, 311–334. https://doi.org/10.1093/petrology/13.2.311.

Lambart, S., Baker, M. B. & Stolper, E. M. (2016). Journal of geophysical research : solid earth. *Journal of Geophysical Research: Solid Earth* **121**, 5708–5735. https://doi.org/10.1002/2015JB012762.

Lambart, S., Laporte, D., Provost, A. & Schiano, P. (2012). Fate of pyroxenite-derived melts in the peridotitic mantle: thermodynamic and experimental constraints. *Journal of Petrology* **53**, 451–476. https://doi.org/10.1093/petrology/egr068.

Lambart, S., Laporte, D. & Schiano, P. (2009). An experimental study of pyroxenite partial melts at 1 and 1.5 GPa: implications for the major-element composition of Mid-Ocean Ridge Basalts. *Earth and Planetary Science Letters* **288**, 335–347. https://doi.org/10.1016/j.epsl.2009.09.038.

Lara, M. & Dasgupta, R. (2020). Partial melting of a depleted peridotite metasomatized by a MORB-derived hydrous silicate melt—implications for subduction zone magmatism. *Geochimica et Cosmochimica Acta* **290**, 137–161. https://doi.org/10.1016/j.gca.2020.09.001.

Li, H., Hermann, J. & Zhang, L. (2022). Melting of subducted slab dictates trace element recycling in global arcs. *Science Advances* **8**, eabh2166. https://doi.org/10.1126/sciadv.abh2166.

Mallik, A. & Dasgupta, R. (2012). Reaction between MORB-eclogite derived melts and fertile peridotite and generation of ocean island basalts. *Earth and Planetary Science Letters* **329–330**, 97–108. https://doi.org/10.1016/j.epsl.2012.02.007.

Mallik, A., Dasgupta, R., Tsuno, K. & Nelson, J. (2016). Effects of water, depth and temperature on partial melting of mantle-wedge fluxed by hydrous sediment-melt in subduction zones. *Geochimica et Cosmochimica Acta* **195**, 226–243. https://doi.org/10.1016/j.gca.2016.08.018.

Mallik, A., Lambart, S. & Chin, E. J. (2021). Tracking the evolution of magmas from heterogeneous mantle sources to eruption. Mantle Convection and Surface Expressions. *Geophysical Monograph* **263**, 153–176. https://doi.org/10.1002/9781119528609.ch6.

Mallik, A., Nelson, J. & Dasgupta, R. (2015). Partial melting of fertile peridotite fluxed by hydrous rhyolitic melt at 2–3 GPa: implications for mantle wedge hybridization by sediment melt and generation of ultrapotassic magmas in convergent margins. *Contributions to Mineralogy and Petrology* **169**. https://doi.org/10.1007/s00410-015-1139-2.

Marschall, H. R. & Schumacher, J. C. (2012). Arc magmas sourced from mélange diapirs in subduction zones. *Nature Geoscience* **5**, 862–867. https://doi.org/10.1038/ngeo1634.

Martin, H., Smithies, R. H., Rapp, R., Moyen, J. F. & Champion, D. (2005). An overview of adakite, tonalite–trondhjemite–granodiorite (TTG), and sanukitoid: relationships and some implications for crustal evolution. *Lithos* **79**, 1–24.

Mcdonough, W. F. & Rudnick, R. L. (1998). Mineralogy and composition of the upper mantle. *Reviews in Mineralogy* **37**, 139–164.

McDonough, W. F. & Sun, S. S. (1995). The composition of the earth. *Chemical Geology* **120**, 223–253. https://doi.org/10.1016/0009-2541(94)00140-4.

Miller, D. M. & Goldstein, S. L. (1994). The continents. **368**, 1–7.

Miller, N. C. & Behn, M. D. (2012). Timescales for the growth of sediment diapirs in subduction zones. *Geophysical Journal International* **190**, 1361–1377. https://doi.org/10.1111/j.1365-246X.2012.05565.x.

Nielsen, S. G. & Marschall, H. R. (2017). Geochemical evidence for mélange melting in global arcs. *Science Advances* **3**, e1602402–e1602407. https://doi.org/10.1126/sciadv.1602402.

O'Neill, H. S. C. & wall, V. J. (1987). The Olivine-orthopyroxene-spinel oxygen geobarometer, the nickel precipitation curve, and the oxygen fugacity of the Earth's Upper Mantle. *Journal of Petrology* **28**, 1169–1191. https://doi.org/10.1093/petrology/28.6.1169.

Parolari, M., Gómez-Tuena, A., Cavazos-Tovar, J. G. & Hernández-Quevedo, G. (2018). A balancing act of crust creation and destruction along the western Mexican convergent margin. *Geology* **46**, 455–458. https://doi.org/10.1130/G39972.1.

Parolari, M., Gómez-Tuena, A., Errázuriz-Henao, C. & Cavazos-Tovar, J. G. (2021). Orogenic andesites and their link to the continental rock cycle. *Lithos* **382-383**, 105958–105383. https://doi.org/10.1016/j.lithos.2020.105958.

Perrillat, J. P., Daniel, I., Lardeaux, J. M. & Cardon, H. (2003). Kinetics of the coesite-quartz transition: application to the exhumation of ultrahigh-pressure rocks. *Journal of Petrology* **44**, 773–788. https://doi.org/10.1093/petrology/44.4.773.

Pirard, C. & Hermann, J. (2015). Focused fluid transfer through the mantle above subduction zones. *Geology* **43**, 915–918. https://doi.org/10.1130/G37026.1.

Plank, T., Cooper, L. & Manning, C. (2009). Emerging geothermometers for estimating slab surface temperatures. *Nature Geoscience* **2**, 611–615. https://doi.org/10.1038/ngeo614.

Plank, T., Kelley, K. A., Zimmer, M. M., Hauri, E. H. & Wallace, P. J. (2013). Why do mafic arc magmas contain ∼4 wt % water on average? How much water comes out arc volcanoes? *Earth and Planetary Science Letters* **364**, 168–179. https://doi.org/10.1016/j.epsl.2012.11.044.

Plank, T. & Langmuir, C. H. (1993). Tracing trace elements from sediment input to volcanic output at subduction zones. *Nature* **362**, 739–743. https://doi.org/10.1038/362739a0.

Portnyagin, M., Bindeman, I., Hoernle, K. & Hauff, F. (2007). Geochemistry of primitive lavas of the Central Kamchatka depression: magma generation at the edge of the Pacific Plate. *Volcanism and Subduction: The Kamchatka Region* , 199–239. https://doi.org/10.1029/172GM16.

Price, R. C., Gamble, J. A., Smith, I. E. M., Maas, R., Waight, T., Stewart, R. B. & Woodhead, J. (2012). The anatomy of an andesite volcano: a time-stratigraphic study of andesite petrogenesis and crustal evolution at Ruapehu Volcano, New Zealand. *Journal of Petrology* **53**, 2139–2189. https://doi.org/10.1093/petrology/egs050.

Rapp, P. & Watson, B. (1995). Dehydration melting of metabasalt at 8-32 kbar: implications for continental growt and crust-mantle recycling. *Journal of Petrology* **36**, 891–931. https://doi.org/10.1093/petrology/36.4.891.

Rapp, R. P., Shimizu, N., Norman, M. D. & Applegate, G. S. (1999). Reaction between slab-derived melts and peridotite in the mantle wedge: experimental constraints at 3.8 GPa. *Chemical Geology* **160**, 335–356. https://doi.org/10.1016/S0009-2541(99)00106-0.

Ringwood, A. E. (1974). The petrological evolution of island arc systems. *Journal of the Geological Society* **130**, 183–204. https://doi.org/10.1144/gsjgs.130.3.0183.

Ruscitto, D. M., Wallace, P. J., Cooper, L. B. & Plank, T. (2012). Global variations in H2O/Ce: 2. Relationships to arc magma geochemistry and volatile fluxes. *Geochemistry, Geophysics, Geosystems* **13**. https://doi.org/10.1029/2011GC003887.

Schmidt, M. W. & Jagoutz, O. (2017). The global systematics of primitive arc melts. *Geochemistry, Geophysics, Geosystems* **18**, 2817–2854. https://doi.org/10.1002/2016GC006699.

Sekine, T. & Wyllie, P. J. (1983). Experimental simulation of mantle hybridization in subduction zones author. *Geology* **91**, 511–528.

Sisson, T. W. & Kelemen, P. B. (2018). Near-solidus melts of MORB + 4 wt% H2O at 0.8–2.8 GPa applied to issues of subduction magmatism and continent formation. *Contributions to Mineralogy and Petrology* **173**(70), 1–23.

Sisson, T. W., Salters, V. J. M. & Larson, P. B. (2014). Petrogenesis of Mount Rainier andesite: magma flux and geologic controls on the contrasting differentiation styles at stratovolcanoes of the southern Washington cascades. *Bulletin of the Geological Society of America* **126**, 122–144. https://doi.org/10.1130/B30852.1.

Søager, N., Portnyagin, M., Hoernle, K., Holm, P. M., Hauff, F. & Garbe-Schönberg, D. (2015). Journal of olivine major and trace element compositions in Southern Payenia Basalts , Argentina: evidence for Pyroxenite—peridotite melt mixing in a Back-arc setting. *Journal of Petrology* **56**, 1495–1518. https://doi.org/10.1093/petrology/egv043.

Sobolev, A. V., Hofmann, A. W., Sobolev, S. V. & Nikogosian, I. K. (2005). An olivine-free mantle source of Hawaiian shield basalts. *Nature* **434**, 590–597. https://doi.org/10.1038/nature03411.

Straub, S. M., Gómez-Tuena, A., Bindeman, I. N., Bolge, L. L., Brandl, P. A., Espinasa-Perena, R., Solari, L., Stuart, F. M., Vannucchi, P. & Zellmer, G. F. (2015). Crustal recycling by subduction erosion in the central Mexican Volcanic Belt. *Geochimica et Cosmochimica Acta* **166**, 29–52. https://doi.org/10.1016/j.gca.2015.06.001.

Straub, S. M., Gomez-Tuena, A., Stuart, F. M., Zellmer, G. F., Espinasa-Perena, R., Cai, Y. & Iizuka, Y. (2011). Formation of hybrid arc andesites beneath thick continental crust. *Earth and Planetary Science Letters* **303**, 337–347. https://doi.org/10.1016/j.epsl.2011.01.013.

Straub, S. M., Gómez-tuena, A., Zellmer, G. F., Espinasa-perena, R., Stuart, F. M., Cai, Y., Langmuir, C. H., Martin-Del Pozzo, A. L. & Mesko, G. T. (2013). The processes of melt differentiation in arc volcanic rocks: insights from OIB-type arc magmas in the central Mexican volcanic belt. *Journal of Petrology* **54**, 665–701. https://doi.org/10.1093/petrology/egs081.

Straub, S. M., LaGatta, A. B., Martin-Del Pozzo, A. L. & Langmuir, C. H. (2008). Evidence from high-Ni olivines for a hybridized peridotite/pyroxenite source for orogenic andesites from the central Mexican Volcanic Belt. *Geochemistry, Geophysics, Geosystems* **9**. https://doi.org/10.1029/2007GC001583.

Straub, S. M., Zellmer, G. F., Gómez-Tuena, A., Espinasa-Pereñ, A. R., Martin-Del Pozzo, A. L., Stuart, F. M. & Langmuir, C. H. (2014). A genetic link between silicic slab components and calc-alkaline arc volcanism in central Mexico. *Geological Society Special Publication* **385**, 31–64. https://doi.org/10.1144/SP385.14.

Syracuse, E. M., van Keken, P. E., Abers, G. A., Suetsugu, D., Bina, C., Inoue, T., Wiens, D. & Jellinek, M. (2010). The global range of subduction zone thermal models. *Physics of the Earth and Planetary Interiors* **183**, 73–90. https://doi.org/10.1016/j.pepi.2010.02.004.

Tatsumi, Y. (1982). Origin of high-magnesian andesites in the Setouchi volcanic belt, Southwest Japan, II. Melting phase relations at high pressures. *Earth and Planetary Science Letters* **60**, 305–317. https://doi.org/10.1016/0012-821X(82)90009-7.

Tatsumi, Y. & Ishizaka, K. (1982). Origin of high-magnesian andesites in the Setouchi volcanic belt, Southwest Japan, I. Petrographical and chemical characteristics. *Earth and Planetary Science Letters* **60**, 293–304. https://doi.org/10.1016/0012-821X(82)90008-5.

Tenner, T. J., Hirschmann, M. M. & Humayun, M. (2012). The effect of H2O on partial melting of garnet peridotite at 3.5 GPa. *Geochemistry, Geophysics, Geosystems* **13**. https://doi.org/10.1029/2011GC003942.

Turner, S. J. & Langmuir, C. H. (2022). A quantitative framework for global variations in arc geochemistry. *Earth and Planetary Science Letters* **584**, 117411. https://doi.org/10.1016/j.epsl.2022.117411.

Ulmer, P., Kaegi, R. & Müntener, O. (2018). Experimentally derived intermediate to silica-rich arc magmas by fractional and equilibrium crystallization at 1·0 GPa: an evaluation of phase relationships, compositions, liquid lines of descent and oxygen fugacity. *Journal of Petrology* **59**, 11–58. https://doi.org/10.1093/petrology/egy017.

Walter, M. (1998). Melting of garnet peridotite and the origin of komatiite and depleted lithosphere. *Journal of Petrology* **39**, 29–60. https://doi.org/10.1093/petroj/39.1.29.

Wang, Y. & Foley, S. F. (2018). Hybridization melting between continent-derived sediment and depleted peridotite in subduction zones. *Journal of Geophysical Research: Solid Earth* **123**, 3414–3429. https://doi.org/10.1029/2018JB015507.

Wood, B. J. & Turner, S. P. (2009). Origin of primitive high-mg andesite: constraints from natural examples and experiments. *Earth and Planetary Science Letters* **283**, 59–66. https://doi.org/10.1016/j.epsl.2009.03.032.

Xu, Y. (2000). Distribution of trace elements in spinel and garnet peridotites. *Science in China, Series D: Earth Sciences* **43**, 166–175. https://doi.org/10.1007/BF02878146.

Yaxley, G. M. & Green, D. H. (1998). Reactions between eclogite and peridotite: mantle refertilisation by subduction of oceanic crust. *Schweizerische Mineralogische und Petrographische Mitteilungen* **78**, 243–255.

Yogodzinski, G. M., Brown, S. T., Kelemen, P. B., Vervoort, J. D., Portnyagin, M., Sims, K. W. W., Hoernle, K., Jicha, B. R. & Werner, R. (2015). The role of subducted basalt in the source of island arc magmas: evidence from seafloor lavas of the Western Aleutians. *Journal of Petrology* **56**, 441–492. https://doi.org/10.1093/petrology/egv006.

Yogodzinski, G. M., Volynets, O. N., Koloskov, A. V., Seliverstov, N. I. & Matvenkov, V. V. (1994). Magnesian andesites and the subduction component in a strongly calc-alkaline series at piip volcano, far western Aleutians. *Journal of Petrology* **35**, 163–204. https://doi.org/10.1093/petrology/35.1.163.

Zamboni, D., Trela, J., Gazel, E., Sobolev, A. V., Cannatelli, C., Lucchi, F., Batanova, V. G. & De Vivo, B. (2017). New insights into the Aeolian Islands and other arc source compositions from high-precision olivine chemistry. *Lithos* **272–273**, 185–191. https://doi.org/10.1016/j.lithos.2016.12.004.

Zhang, N., Behn, M. D., Parmentier, E. M. & Kincaid, C. (2020a). Melt segregation and depletion during ascent of buoyant diapirs in subduction zones. *Journal of Geophysical Research: Solid Earth* **125**, 1–21. https://doi.org/10.1029/2019JB018203.

Zhang, Y., Liang, X., Wang, C., Jin, Z., Zhu, L. & Gan, W. (2020b). Experimental constraints on the partial melting of sediment-metasomatized lithospheric mantle in subduction zones. *American Mineralogist* **105**, 1191–1203. https://doi.org/10.2138/am-2020-7403.